Resolving the fibrotic niche of human liver cirrhosis at single-cell level

Resolving the fibrotic niche of human liver cirrhosis using single-cell transcriptomics

Ramachandran P[1]*, Dobie R[1], Wilson-Kanamori JR[1], Dora EF[1], Henderson BEP[1], Luu NT[2,3], Portman JR[1], Matchett KP[1], Brice M[1], Marwick JA[1,4], Taylor RS[1], Efremova M[5], Vento-Tormo R[5], Carragher NO[4], Kendall TJ[1,6], Fallowfield JA[1], Harrison EM[7], Mole DJ[1,7], Wigmore SJ[1,7], Newsome PN[2,3], Weston CJ[2,3], Iredale JP[8], Tacke F[9], Pollard JW[10,11], Ponting CP[12], Marioni JC[5,13,14], Teichmann SA[5,13,15], Henderson NC[1]*

[1]University of Edinburgh Centre for Inflammation Research, The Queen's Medical Research Institute, Edinburgh BioQuarter, Edinburgh, UK.
[2]NIHR Birmingham Biomedical Research Centre, University Hospitals Birmingham NHS Foundation Trust and University of Birmingham, UK
[3]Institute of Immunology and Immunotherapy, University of Birmingham, UK
[4]Cancer Research UK Edinburgh Centre, MRC Institute of Genetics and Molecular Medicine at the University of Edinburgh, Edinburgh, UK.
[5]Wellcome Sanger Institute, Wellcome Genome Campus, Hinxton, Cambridge, UK.
[6]Division of Pathology, University of Edinburgh, Edinburgh, UK.
[7]Clinical Surgery, University of Edinburgh, Royal Infirmary of Edinburgh, Edinburgh, UK.
[8]Office of the Vice Chancellor, Beacon House and National Institute for Health Research, Biomedical Research Centre, Bristol, UK
[9]Department of Hepatology and Gastroenterology, Charité University Medical Center, Berlin, Germany
[10]MRC Centre for Reproductive Health, The Queen's Medical Research Institute, University of Edinburgh, Edinburgh, UK.
[11]Department of Developmental and Molecular Biology, Albert Einstein College of Medicine, New York, USA.
[12]MRC Human Genetics Unit, MRC Institute of Genetics and Molecular Medicine at the University of Edinburgh, Edinburgh, UK.
[13]European Molecular Biology Laboratory, European Bioinformatics Institute (EMBL-EBI), Hinxton, Cambridge, UK.
[14]Cancer Research UK Cambridge Institute, University of Cambridge, Li Ka Shing Centre, Cambridge, UK.
[15]Theory of Condensed Matter Group, The Cavendish Laboratory, University of Cambridge, JJ Thomson Ave, Cambridge, CD3 0EH, UK.

*Address correspondence to:

Prakash Ramachandran, University of Edinburgh Centre for Inflammation Research, The Queen's Medical Research Institute, Edinburgh BioQuarter, 47 Little France Crescent, Edinburgh, UK, EH16 4TJ. Phone: 0131.242.6654; Email: Prakash.Ramachandran@ed.ac.uk or Neil Henderson, University of Edinburgh Centre for Inflammation Research, The Queen's Medical Research Institute, Edinburgh BioQuarter, 47 Little France Crescent, Edinburgh, UK, EH16 4TJ. Phone: 0131.242.6688; Email: Neil.Henderson@ed.ac.uk

Abstract

Currently there are no effective antifibrotic therapies for liver cirrhosis, a major killer worldwide. To obtain a cellular resolution of directly-relevant pathogenesis and to inform therapeutic design, we profile the transcriptomes of over 100,000 primary human single cells, yielding molecular definitions for the major non-parenchymal cell types present in healthy and cirrhotic human liver. We uncover a novel scar-associated $TREM2^{+}CD9^{+}$ macrophage subpopulation, which expands in human and mouse liver fibrosis, has a distinct differentiation trajectory from circulating monocytes and displays a pro-fibrogenic phenotype. In the endothelial compartment, we show that newly-defined $ACKR1^{+}$ and $PLVAP^{+}$ endothelial cells expand in cirrhosis, are topographically located in the fibrotic septae and enhance leucocyte transmigration. Multi-lineage ligand-receptor modelling of specific interactions between the novel scar-associated macrophages, endothelial cells and $PDGFR\alpha^{+}$ collagen-producing mesenchymal cells in the fibrotic niche, reveals intra-scar activity of several major pro-fibrogenic pathways including TNFRSF12A, PDGFR and NOTCH signalling. Our work dissects unanticipated aspects of the cellular and molecular basis of human organ fibrosis at a single-cell level, and provides the conceptual framework required to discover rational therapeutic targets in liver cirrhosis.

Main

Liver cirrhosis is a major global healthcare burden. Recent estimates suggest that 844 million people worldwide have chronic liver disease, with a mortality rate of two million deaths per year and a rising incidence[1]. In health, the liver serves a myriad of functions including detoxification, metabolism, bile production and immune surveillance. Chronic liver disease, the result of iterative liver injury secondary to any cause, results in progressive fibrosis, disrupted hepatic architecture, vascular changes and aberrant regeneration, defining characteristics of liver cirrhosis[2]. Importantly, the degree of liver fibrosis predicts adverse patient outcomes, including the development of cirrhosis-related complications, hepatocellular carcinoma and death[3]. Hence, there is a clear therapeutic imperative to develop effective anti-fibrotic approaches for patients with chronic liver disease[4–7].

Liver fibrosis involves a complex, orchestrated interplay between multiple non-parenchymal cell (NPC) lineages including immune, endothelial and mesenchymal cells spatially located within areas of scarring, termed the fibrotic niche. Despite rapid progress in our understanding of the cellular interactions underlying liver fibrogenesis accrued using rodent models, there remains a significant 'translational gap' between putative targets and effective patient therapies[4,5]. This is in part due to the very limited definition of the functional heterogeneity and interactome of cell lineages that contribute to the fibrotic niche of human liver cirrhosis, which is imperfectly recapitulated by rodent models[4,6].

Single-cell RNA sequencing (scRNA-seq) has the potential to deliver a step change in both our understanding of healthy tissue homeostasis as well as disease pathogenesis, allowing the interrogation of individual cell populations at unprecedented resolution[8–11]. Here, we have studied the mechanisms regulating human liver cirrhosis, using scRNA-seq to analyse the transcriptomes of 106,616 single cells obtained from ten healthy and cirrhotic human livers and peripheral blood.

Our data define: (1) a single-cell atlas of non-parenchymal cells in healthy and cirrhotic human liver; (2) a new subpopulation of scar-associated $TREM2^{+}CD9^{+}$ pro-fibrogenic macrophages; (3) new subpopulations of scar-associated $ACKR1^{+}$ and $PLVAP^{+}$

endothelial cells; and (4) key ligand-receptor interactions between novel scar-associated macrophages, endothelial subpopulations and collagen-producing myofibroblasts in the fibrotic niche. Thus, we have simultaneously identified a series of intra-scar pro-fibrogenic pathways which represent hitherto unsuspected therapeutic targets for the treatment of liver fibrosis, whilst demonstrating the applicability of scRNA-seq to define pathogenic mechanisms for other human fibrotic disorders.

Results

Single-cell atlas of human liver non-parenchymal cells

Hepatic NPC were isolated from fresh healthy and cirrhotic human liver tissue spanning a range of aetiologies of cirrhosis (Fig. 1a, Extended Data Fig. 1a). Importantly, to minimise artefacts[12], we developed a rapid tissue processing pipeline, obtaining fresh non-ischaemic liver tissue taken by wedge biopsy prior to the interruption of the hepatic vascular inflow during liver surgery or transplantation, and immediately processing this for FACS. This enabled a workflow time of under three hours from patient to single-cell droplet encapsulation (Methods).

We used an unbiased approach, FACS sorting viable single cells from liver tissue into broad leucocyte ($CD45^+$) or other NPC ($CD45^-$) fractions (Extended Data Fig. 1b), prior to scRNA-seq. To facilitate discrimination between liver-resident and circulating leucocytes, we also performed scRNA-seq on $CD45^+CD66b^-$ peripheral blood mononuclear cells (PBMCs) (Extended Data Fig. 1c, f). In total, we analysed 67,494 human cells from healthy (n=5) and cirrhotic (n=5) livers, 30,741 PBMCs from cirrhotic patients (n=4) and compared our data with a publicly-available reference dataset of 8,381 PBMCs from a healthy donor.

Tissue cells and PBMCs could be partitioned into 21 distinct clusters, which we visualized using *t*-distributed stochastic neighbourhood embedding (t-SNE) (Extended Data Fig. 1d). Clusters were annotated using signatures and integrating with known lineage markers (Extended Data Fig. 1e; signature gene lists available in Supplementary Table 1). All PBMC datasets contained the major blood lineages, with excellent reproducibility between samples (Extended Data Fig. 1g, h). To generate an atlas of

liver-resident cells, contaminating circulating cells were removed from the liver tissue datasets, by excluding individual cells from the tissue samples which mapped transcriptionally to blood-derived clusters 1 and 13 (Extended Data Fig. 1d).

Re-clustering the 66,135 liver-resident cells revealed 21 clusters (Fig. 1b), each containing cells from both healthy and cirrhotic livers (Fig. 1c). Gene signature analysis enabled annotation of each cluster by major cell lineage (Fig. 1d, Extended Data Fig. 2a, b). We noted heterogeneity in the post-normalised detected number of genes and unique molecular identifiers (UMIs) per cell, dependent on cell lineage (Extended Data Fig. 2c, d). All samples contained the expected cell lineages (Extended Data Fig. 2e, g) and reproducibility between livers was excellent for the main NPC populations (Extended Data Fig. 2f).

We used an area-under-curve classifier to identify cell subpopulation markers across all 21 clusters and 11 lineages (Fig. 1e; Supplementary Tables 2 and 3). Expression of collagens type I and type III, the main extracellular matrix components of the fibrotic niche, was restricted to cells of the mesenchymal lineage (Fig. 1e). To gain further resolution on NPC heterogeneity, we then iterated clustering and marker gene identification on each lineage in turn, for example defining 11 clusters of T cells and innate lymphoid cells (ILCs) (Extended Data Fig. 3a) and four clusters of B cells and plasma cells (Extended Data Fig. 3f, g, Supplementary Table 6). No major differences in B cell or plasma cell composition between healthy and cirrhotic livers were observed (Extended Data Fig. 3h), and plasmacytoid dendritic cells (pDC) showed no additional heterogeneity.

To further annotate the 11 T cell and ILC clusters (36,900 cells from 10 livers) we assessed expression of known markers (Extended Data Fig. 3c) and computationally identified differential marker genes (Extended Data Fig. 3d, Supplementary Table 4). We also performed imputation of gene dropouts, which enhanced detection of discriminatory marker genes for each cluster but did not yield additional T cell or ILC subpopulations (Extended Data Fig. 3e, Supplementary Table 5). All T cell and ILC clusters expressed tissue residency markers *CD69* and *CXCR4*. Clusters 1 and 2 were $CD4^+$ T cells, with $CD4^+$ T cell(2) expanding significantly in cirrhotic livers (Extended Data Fig. 3a, b, e) and expressing *SELL* and *CCR7,* indicating an expansion of memory

CD4$^+$ T cells in liver cirrhosis. Sparse expression of *FOXP3, RORC*, *IL17A* and *IFNG* in both CD4$^+$ T cell subpopulations suggested the presence of Tregs, Th17 and Th1 cells in these clusters. Clusters 3, 4 and 5 were CD8$^+$ T cells, with features of effector T cells expressing *GZMA*, *GZMH* and *IFNG*. Two resident CD56^{bright} IL7R$^-$ NK cell clusters were defined (NK cell(1) and NK cell(2)), as well as a distinct cytotoxic CD56^{dim} NK cell population (cNK), with specific expression of *FCGR3A* and *GZMB*. No expansion of these populations was observed in cirrhotic livers.

We provide an interactive gene browser freely-available online (http://www.livercellatlas.mvm.ed.ac.uk), to allow assessment of individual gene expression both in all human liver NPC and in specific lineages, comparing healthy *versus* cirrhotic livers.

(Note to referees: http://www.livercellatlas.mvm.ed.ac.uk will be made freely available. For review purposes, log-in details are username: Edinburghlivercellatlas; password: Cirrhosis; please refresh your browser if the webpage does not load at first attempt.)

Distinct macrophage subpopulations inhabit the fibrotic niche

Macrophages are critical to tissue homeostasis and wound-healing[13]. Previous studies have highlighted phenotypically-distinct macrophage populations orchestrating both liver fibrosis progression and regression in rodent models[14,15], with preliminary evidence of heterogeneity in fibrotic human livers[16]. Here, we define unique subpopulations of macrophages which populate the fibrotic niche of cirrhotic human livers. Unsupervised clustering of all 10,737 mononuclear phagocytes (1,074±153 cells from each liver), isolated from the combined liver-resident cell dataset, identified nine MP clusters and one cluster of proliferating MP cells (Fig. 2a). We annotated these nine clusters as subpopulations of scar-associated macrophages (SAM), Kupffer cells (KC), tissue monocytes (TMo), and conventional dendritic cells (cDC) (Fig. 2a; see below). Strikingly, clusters MP(4) and MP(5), named SAM(1) and SAM(2) respectively, were expanded in cirrhotic livers (Fig. 2b), a finding that was confirmed by quantification of the MP cell composition of each liver individually (Fig. 2c), and reproduced in all cirrhotic livers irrespective of liver disease aetiology.

To enable MP cell annotation, we initially assessed expression of known MP marker genes (Extended Data Fig. 4a), classifying clusters MP(8) and MP(9) as conventional dendritic cells, cDC2 and cDC1 respectively, based on *CD1C* and *CLEC9A* specificity. However, the remaining markers did not demarcate the other monocyte and macrophage subpopulations. Instead, these were identified using differential expression analysis across all MP clusters (Fig. 2d, Supplementary Table 7). Clusters MP(1), MP(2) and MP(3) were distinguished by expression of S100 genes, *FCN1, MNDA* and *LYZ*, in keeping with a tissue monocyte (TMo) phenotype and informing annotation as TMo(1), TMo(2) and TMo(3) respectively (Fig. 2d, e, Extended Data Fig. 4a, Supplementary Table 7).

Clusters MP(6) and MP(7) were enriched in *CD163*, *MARCO*, *TIMD4* and *CD5L* (Extended Data Fig. 4b); multiplex immunofluorescence staining confirmed these as Kupffer cells (KC; resident liver macrophages), facilitating annotation of these clusters as KC(1) and KC(2) respectively (Extended Data Fig. 4c). Application of these markers enabled the definitive distinction between KC and other MP cells for the first time in human liver tissue. KC displayed characteristic morphology and sinusoidal topography in healthy livers but were absent from areas of scarring in cirrhotic livers (Extended Data Fig. 4c). A lack of *TIMD4* expression distinguished KC(2) from KC(1) (Extended Data Fig. 4b); $CD163^{+}MARCO^{+}TIMD4^{-}$ cells were identifiable in healthy livers but rare in cirrhotic livers (Extended Data Fig. 4c), concordant with a significant reduction of KC(2) cells in cirrhosis (Fig. 2c). Automated histological cell counting demonstrated $TIMD4^{+}$ cell numbers to be equivalent between healthy and cirrhotic livers, but showed a loss of $MARCO^{+}$ cells, consistent with selective reduction in $MARCO^{+}TIMD4^{-}$ KC in liver fibrosis (Extended Data Fig. 4d, e).

Scar-associated clusters SAM(1) and SAM(2), expanded in diseased livers and expressed the unique markers *TREM2* and *CD9* (Fig. 2c-e). These newly-defined macrophages displayed a hybrid phenotype, with features of both tissue monocytes and KC (Fig. 2d, e), analogous to monocyte-derived macrophages in murine liver injury models[15,17]. Multi-colour flow cytometry confirmed expansion of these $TREM2^{+}CD9^{+}$ macrophages in human fibrotic livers (Fig. 2f, Extended Data Fig. 4f). Tissue immunofluorescence staining and single-molecule fluorescent in situ hybridization

(smFISH) demonstrated the presence of TREM2$^+$MNDA$^+$ and CD9$^+$MNDA$^+$ macrophages in fibrotic livers (Extended Data Fig. 4g-i). Multiplex immunofluorescence further confirmed the presence of TREM2$^+$CD9$^+$ cells localised in collagen-positive scar regions in cirrhotic livers (Fig. 2g), and automated cell counting of stained sections confirmed expansion of TREM2$^+$ and CD9$^+$ cells in cirrhotic livers (Fig. 2h, i).

Strikingly, TREM2$^+$ and CD9$^+$ cells were rarely identified in the parenchyma of healthy livers, but were consistently located within areas of scar in cirrhotic livers. To confirm this, automated cell counting was applied to immunohistochemically-stained cirrhotic livers morphologically segmented into regions of fibrotic septae and parenchymal nodules (Fig. 2j). This demonstrated a significant accumulation of TREM2$^+$ and CD9$^+$ cells in fibrotic regions, whilst negligible numbers of KC populated the fibrotic septae (Fig. 2j). Hence, we annotated TREM2$^+$CD9$^+$ MP cells as scar-associated macrophages (SAM).

Local proliferation has been shown to play a significant role in the expansion of macrophage subpopulations at sites of inflammation and fibrosis in experimental rodent models[15,18,19], but has not been extensively characterised in human inflammatory disorders. To investigate MP proliferation in human liver fibrosis, we isolated the cycling MP cluster (Fig. 2a; cluster 10), which was enriched for multiple cell cycle-related genes (Supplementary Table 7). Cycling MP cells subclustered into four, yielding cDC1, cDC2, KC and SAM subpopulations (Extended Data Fig. 4j). We observed a significant expansion of cycling SAM in cirrhosis, representing 1.70±0.52% of total TREM2$^+$ MP cells in cirrhotic livers (Extended Data Fig. 4k). In contrast 0.99±0.63% of KC were proliferating in healthy livers, with none detected in cirrhotic livers (Extended Data Fig. 4k). These data highlight the potential role of local macrophage proliferation in driving the accumulation of SAM in the fibrotic niche of human chronic liver disease.

Pro-fibrogenic phenotype of scar-associated macrophages

To delineate the functional profile of SAM we generated self-organising maps using the *SCRAT* package, visualising co-ordinately expressed gene groups across the MP

subpopulations. This created a landscape of 3600 metagenes on a 60x60 grid and highlighted 44 metagene signatures overexpressed in the MP lineage (Fig. 3a). Mapping the nine MP cell clusters to this landscape (Extended Data Fig. 5a) identified six optimally-differentiating metagene signatures, denoted as A-F (Fig. 3a, Supplementary Table 8). Signatures A and B defined the scar-associated macrophages and were enriched for ontology terms relevant to tissue fibrosis and associated processes such as angiogenesis, in addition to known macrophage functions such as phagocytosis and antigen processing (Fig. 3b). These SAM-defining signatures included genes such as *TREM2*, *IL1B*, *SPP1*, *LGALS3*, *CXCR4*, *CCR2*, and *TNFSF12*; a number of which are known to regulate the function of scar-producing myofibroblasts in fibrotic liver diseases[20–25]. The remaining MP subpopulations were defined by signature C (KC), signatures D, E (TMo) and signature F (cDC1); ontology terms matched known functions for the associated cell type (Fig. 3b, Extended Data Fig. 5b, Supplementary Table 8). In particular, the KC clusters showed significant enrichment for ontology terms involving endocytosis, lipid and iron homeostasis, known functions of KC in mice[26]. Importantly, macrophage populations did not conform to either an M1 or M2 phenotype, again highlighting the limitation of this classification.

In mice, there are two main origins of hepatic macrophages, either embryologically-derived or monocyte-derived[27]. Under homeostatic conditions, tissue-resident KC predominate and are embryologically-derived self-renewing cells[28–32]. However, following liver injury, macrophages derived from the recruitment and differentiation of circulating monocytes accumulate in the liver and regulate hepatic fibrosis[15,33]. The ontogeny of human hepatic macrophage subpopulations has never previously been investigated. Scar-associated $TREM2^{+}CD9^{+}$ macrophages demonstrated a monocyte-like morphology (Fig. 2g, Extended Data Fig. 4g-i) and a distinct topographical distribution from KC (Fig. 2j), suggesting they may represent monocyte-derived cells. To computationally assess the origin of these SAM, we performed *in silico* trajectory analysis on a combined dataset of peripheral blood monocytes and liver-resident MPs. We visualised the transcriptional profile of these cells using a diffusion map, mapped them along a pseudotemporal trajectory (using the *monocle* R package) and interrogated their directionality via spliced and unspliced mRNA ratios (RNA velocity[34,35]) (Fig. 3c). These analyses suggested a branching differentiation trajectory from peripheral

blood monocytes into either SAM or cDC (Fig. 3c). Additionally, applying RNA velocity indicated a lack of differentiation from KC to SAM, and no progression from SAM to KC (Fig. 3c).

To further investigate the pseudotemporal relationship between SAM and KC, we visualised the combined blood monocyte and liver-resident MP dataset using a UMAP, and performed additional RNA velocity analyses[34,35] (Fig. 3d). Evaluation of spliced and unspliced mRNAs showed expected downregulation (negative velocity) of monocyte gene *MNDA* in SAM, expected upregulation (positive velocity) of SAM marker gene *CD9* in tissue monocytes, and a lack of KC gene *TIMD4* velocity in SAM (Fig. 3e). This infers an absence of pseudotemporal dynamics between KC and SAM. Furthermore, assessment of the probabilities of cells in this dataset transitioning into SAM, indicated a higher likelihood of tissue monocytes than KC differentiating into SAM (Fig. 3f). Overall, these data suggest that scar-associated macrophages in human fibrotic liver are monocyte-derived, and imply that SAM represent a terminally-differentiated cell state within the fibrotic niche.

To further characterise the phenotype of scar-associated macrophages, we identified differentially expressed genes along the branching monocyte differentiation trajectories (Fig. 3g). We defined three gene co-expression modules by hierarchical clustering, with module 1 representing genes that are upregulated during blood monocyte-to-SAM differentiation (Fig. 3g). Module 1 was over-expressed in SAM, and contained multiple pro-fibrogenic genes including *SPP1*, *LGALS3*, *CCL2*, *CXCL8*, *PDGFB* and *VEGFA*[20–23,36–38](Fig. 3h). Analogous to signatures A and B (Fig. 3b), module 1 displayed ontology terms consistent with promoting tissue fibrosis and angiogenesis, including the regulation of other relevant cell types such as fibroblasts and endothelial cells (Fig. 3h). Co-expression module 2 contained genes that were downregulated during monocyte-to-SAM differentiation, confirming a loss of characteristic monocyte genes (Extended Data Fig. 5e). Module 3 encompassed a distinct group of genes that were upregulated during monocyte-to-cDC differentiation (Extended Data Fig. 5f). Full lists of genes and ontology terms for all three modules are available (Supplementary Table 9). These data highlight that SAM acquire a specific pro-fibrogenic phenotype during differentiation from circulating monocytes.

To further assess the function of human SAM, macrophage subpopulations were isolated from cirrhotic human livers by FACS (Fig. 2f, Extended Data Fig. 4f). SAM demonstrated enhanced protein secretion of several of the mediators identified by transcriptional analysis (Extended Data Fig. 5c). Additionally, conditioned media from SAM promoted fibrillar collagen expression by primary human hepatic stellate cells (HSC) (Extended Data Fig. 5d), confirming that SAM have a pro-fibrogenic phenotype.

To enable cross-species comparison, we performed scRNA-seq on liver MP cells isolated from control (uninjured) mice or mice treated with chronic carbon tetrachloride (CCl_4), a well-established mouse model of liver fibrosis[15]. MP cells from fibrotic livers were isolated 24 hours following the final CCl_4 injection, a time of active fibrogenesis[15]. Five clusters of MP cells were defined (Extended Data Fig. 6a), with differentially expressed marker genes (Extended Data Fig. 6c, d, Supplementary Table 10) which facilitated cell type annotation (Extended Data Fig. 6a). An injury-specific macrophage population, cluster mMP(2), was identified (Extended Data Fig. 6a, b) and was differentiated by high expression of *Cd9*, *Trem2*, *Spp1* and *Lgals3* (Extended Data Fig. 6c, d). We confirmed expansion of this murine $CD9^+$ SAM (mSAM) population in liver fibrosis (Extended Data Fig. 6e, f). Co-culture of mSAM with quiescent primary murine HSC promoted fibrillar collagen expression in HSC (Extended Data Fig. 6g), indicating a pro-fibrogenic phenotype of mSAM. To confirm that mSAM represent the corollary population to human SAM (hSAM), we performed an unbiased canonical correlation analysis (CCA) between human and mouse MP datasets[39]. Both hSAM and mSAM clustered together (h&mMP(2); Extended Data Fig. 6h,i) and this cluster was enriched for the SAM markers *CD9*, *TREM2* and *SPP1* (Extended Data Fig. 6j). Similar cross-species conservation was also observed for KC (h&mMP(3); Extended Data Fig. 6h-j).

To identify potential transcriptional regulators of human SAM we used the *SCENIC* package to define sets of genes co-expressed with known transcription factors, termed regulons. We assessed the cell activity score for differentially-expressed regulons along the tissue monocyte-macrophage pseudotemporal trajectory and in KC, allowing visualisation of regulon activity across liver-resident macrophage subpopulations (Extended Data Fig. 5g, h, Supplementary Table 11). This identified regulons and corresponding transcription factors associated with distinct macrophage phenotypes,

highlighting *NR1H3* and *SPIC* activity in human KC (Extended Data Fig. 5g, h), which are known to regulate KC function in mice[40,41]. Scar-associated macrophages are enriched for regulons containing the transcription factors *HES1* and *EGR2* (Extended Data Fig. 5g, h), both of which have been associated with modulation of macrophage phenotype and tissue fibrosis[42–45].

To determine whether SAM also expand in earlier stage human liver disease, we analysed cohorts of patients with non-alcoholic fatty liver disease (NAFLD). We applied differential gene expression signatures of human SAM, KC and TMo to a deconvolution algorithm[46], which enabled the assessment of the hepatic monocyte-macrophage composition in whole liver microarray data across the spectrum of early-stage NAFLD severity[47] (Extended Data Fig. 7a). This demonstrated an expansion of SAM in patients with non-alcoholic steatohepatitis (NASH) (Extended Data Fig. 7a, b), with an increased frequency of SAM with worsening histological NASH activity (NAS) and fibrosis scores (Extended Data Fig. 7c). No association was observed between SAM frequency and patient demographics such as gender, age or body mass index (Extended Data Fig. 7d). We were also able to histologically identify SAM in a locally generated NASH biopsy cohort (Extended Data Fig. 7e). SAM expansion increased with NASH activity (Extended Data Fig. 7e) and there was a positive correlation between SAM number and degree of fibrosis across the full severity spectrum of NAFLD-induced liver fibrosis (Extended Data Fig. 7f).

In summary, multimodal computational, functional and histological analysis demonstrates that TREM2^{+}CD9^{+} scar-associated macrophages derive from the recruitment and differentiation of circulating monocytes, are conserved across species, display a pro-fibrogenic phenotype and expand early in the course of liver disease progression.

Distinct endothelial subpopulations inhabit the fibrotic niche

In rodent models, hepatic endothelial cells are known to regulate both fibrogenesis[48,49] and macrophage recruitment to the fibrotic niche[37]. Unsupervised clustering of human liver endothelial cells identified seven subpopulations (Fig. 4a). Clusters Endo(6) and Endo(7) significantly expanded in cirrhotic compared to healthy livers, whilst Endo(1)

contracted (Fig. 4a, b). Classical endothelial cell markers did not discriminate between the seven clusters, although Endo(1) was distinct in lacking *CD34* expression (Extended Data Fig. 8a). In order to fully annotate endothelial subpopulations (Extended Data Fig. 8h), we identified differentially expressed markers (Fig. 4c, Supplementary Table 12), determined functional expression profiles (Extended Data Fig. 8g, Supplementary Table 13), performed transcription factor regulon analysis (Fig. 4g, Supplementary Table 14) and assessed spatial distribution via multiplex immunofluorescence staining (Fig. 4d, e).

Disease-specific endothelial cells Endo(6) and Endo(7), $CD34^+PLVAP^+VWA1^+$ and $CD34^+PLVAP^+ACKR1^+$ respectively (Fig. 4c, Extended Data Fig. 8b), expanded in cirrhotic liver tissue (Fig. 4f) and were spatially restricted to the fibrotic niche (Fig. 4d, e, Extended Data Fig. 8c), allowing their annotation as scar-associated endothelia SAEndo(1) and SAEndo(2) respectively. Scar-associated endothelial cells displayed enhanced expression of the *ELK3* regulon (Fig. 4g), a transcription factor known to modulate angiogenesis[50]. Metagene signature analysis found that Endo(6) (SAEndo(1)) cells expressed pro-fibrogenic genes including *PDGFD*, *PDGFB*, *LOX*, *LOXL2* and several basement membrane components[51–53]; associated significant ontology terms included extracellular matrix organization and wound healing (signature A; Extended Data Fig. 8g). Endo(7) (SAEndo(2)) cells displayed an immunomodulatory phenotype (signature B; Extended Data Fig. 8g). Furthermore, the most discriminatory marker for this cluster, ACKR1, is restricted to venules in mice[54] and has a role in regulating leucocyte recruitment[55]. We isolated endothelial cells from healthy and cirrhotic human livers and confirmed increased expression of PLVAP, CD34 and ACKR1 on cells from diseased livers (Extended Data Fig. 8d). Flow-based adhesion assays[56] demonstrated that cirrhotic endothelial cells showed enhanced leucocyte transmigration (Extended Data Fig. 8e), an effect that was attenuated by ACKR1 knockdown (Extended Data Fig. 8f). These data demonstrate that SAEndo regulate inflammatory cell recruitment to the fibrotic niche.

Using *CLEC4M* as a discriminatory marker of cluster Endo(1) (Fig. 4c, Extended Data Fig. 8b), immunofluorescence confirmed these $CLEC4M^+CD34^-$ cells as liver sinusoidal endothelial cells (LSEC), restricted to perisinusoidal cells within the liver

parenchyma (Fig. 4d). Cluster Endo(1) demonstrated known features of LSEC, including *GATA4* transcription factor regulon expression[57] (Fig. 4g), and a metagene signature enriched for ontology terms including endocytosis and immune response[58] (signature D, Extended Data Fig. 8g). There was a reduction in CLEC4M staining in cirrhotic livers with an absence in fibrotic septae (Fig. 4d, f), indicating that LSEC do not inhabit the fibrotic niche in chronic liver disease. This was further supported by trajectory analysis, suggesting a lack of clear pseudotemporal dynamics between the LSEC and clusters SAEndo(1) and SAEndo(2) (Extended Data Fig. 8i).

We annotated cluster Endo(2) ($PDPN^+CD34^+PLVAP^-$) as lymphatic endothelial cells based on marker gene expression, relevant ontology terms (signature E; Extended Data Fig. 8g) and *FOXC2* and *HOXD8* regulon activity (Fig. 4g)[59,60]. Lymphatics populated the portal region of healthy livers (Fig. 4e). Hierarchical clustering of the endothelial subpopulations demonstrated that clusters Endo(3) and Endo(4) were closely related to LSEC (dendrogram not shown), co-expressing markers including *CLEC4G* (Extended Data Fig. 8b). Endo(4), defined as $RSPO3^+CD34^+PLVAP^+$ (Fig. 4c, Extended Data Fig. 8b), expressed a metagene signature overlapping with LSEC (signature D, Extended Data Fig. 8g), and were identified as central vein endothelial cells (Fig. 4e). This mirrors murine liver zonation data indicating RSPO3 as a marker of pericentral endothelial cells[61]. Similar to LSEC, central vein endothelial cells did not inhabit the fibrotic niche in cirrhosis (Fig. 4e).

Cluster Endo(5), $AIF1L^+CD34^+PLVAP^+$ cells, were mapped to periportal thick-walled vessels, consistent with hepatic arterial endothelial cells (Fig. 4e). Of note, these cells were also topographically associated with fibrotic septae in cirrhotic livers (Fig. 4e). The arterial identity of this cluster was further indicated by *SOX17* regulon expression[62] **(**Fig. 4g), and it displayed a metagene signature enriched for Notch pathway ligands *JAG1*, *JAG2* and *DLL4*; ontology terms included animal organ development, angiogenesis and Notch signalling (signature C; Extended Data Fig. 8g) in keeping with the known requirement of the Notch pathway in the development and maintenance of hepatic vasculature[63]. Endo(5) was annotated as HAEndo for subsequent analysis of cellular interactions within the fibrotic niche.

PDGFRA expression defines scar-associated mesenchymal cells

Hierarchical clustering of human liver mesenchymal cells identified four populations, including a population of mesothelial cells (Fig. 5a, b, Extended Data Fig. 9a, Supplementary Table 15). *MYH11* expression distinguished cluster Mes(1) (Fig. 5b, Extended Data Fig. 9a), and labelled a population of vascular smooth muscle cells (VSMC) (Fig. 5c). Cluster Mes(2) expressed high levels of *RGS5* (Fig. 5b, Extended Data Fig. 9a). RGS5 immunofluorescence staining demonstrated that these mesenchymal cells were located peri-sinusoidally (Fig. 5c), identifying this population as hepatic stellate cells (HSC)[64]. RGS5$^+$ cells were absent from the fibrotic niche (Fig. 5c). Cluster Mes(3) was distinguished by *PDGFRA* expression, in addition to high levels of fibrillar collagens and pro-fibrogenic genes such as *TIMP1* and *CCL2* (Fig. 5b, d, Extended Data Fig. 9a). PDGFRα$^+$ cells expanded significantly in cirrhotic livers (Fig. 5a, e, f) and were spatially mapped to the fibrotic niche (Fig. 5f), enabling annotation as scar-associated mesenchymal cells (SAMes).

To study heterogeneity within the SAMes population, further hierarchical clustering was performed on this population (Extended Data Fig. 9b). Two populations of SAMes were identified (Extended Data Fig. 9c, Supplementary Table 16), both of which expanded in cirrhotic livers (Extended Data Fig. 9d). OSR1, a marker of fibroblast subpopulations and regulator of extracellular matrix production[65], distinguished a subpopulation of SAMes (Extended Data Fig. 9c), labelled a population of periportal cells in healthy liver (Extended Data Fig. 9e) and a subpopulation of scar-associated cells in the fibrotic niche (Extended Data Fig. 9f). These OSR1$^+$ cells are likely to represent portal fibroblasts.

In rodent models, HSC differentiate into scar-producing myofibroblasts following parenchymal liver injury[66–68]. We interrogated HSC differentiation in human liver tissue using pseudotemporal ordering and RNA velocity analyses between HSC and SAMes clusters, demonstrating a clear trajectory from HSC to SAMes (Extended Data Fig. 9g). Assessment of gene co-expression modules along the HSC-to-SAMes differentiation continuum indicated upregulation of fibrogenic genes including *COL1A1*, *COL1A2*, *COL3A1, TIMP1, CCL2* and downregulation of genes including

RGS5, *IGFBP5*, *ADAMTS1* and *GEM,* which are known to be downregulated in murine HSC in response to liver injury[67] (Extended Data Fig. 9h).

Resolving the multi-lineage interactome in the fibrotic niche

Having defined the scar-associated macrophage, endothelial and mesenchymal populations, we confirmed the close topographical association of these cells within the fibrotic niche (Fig. 6a, b). To interrogate how these newly-defined cellular subpopulations regulate fibrosis and to identify tractable therapeutic targets, we performed an unbiased ligand-receptor interaction analysis between these scar-associated populations. We used CellPhoneDB, a repository of curated ligand-receptor interactions integrated with a statistical framework. We calculated statistically significant ligand-receptor pairs, based on expression of receptors by one lineage and ligands by another, using empirical shuffling[69].

Numerous statistically significant paracrine and autocrine interactions were detected between ligands and cognate receptors expressed by SAM, SAEndo and SAMes within the fibrotic niche (Supplementary Table 17). We focused further functional analyses on interactions with SAMes, the fibrillar collagen-producing population. Both SAM and SAEndo populations demonstrated multiple interactions that could regulate SAMes function (Extended Data Fig. 10a). In keeping with our data demonstrating that human and murine SAM promote fibrillar collagen expression in HSC (Extended Data Fig. 5d, Extended Fig. 6g), SAM expressed a number of epidermal growth factor receptor (EGFR) ligands which are known to regulate mesenchymal cell activation[70,71]. Additionally, SAM expressed mesenchymal cell mitogens *TNFSF12* and *PDGFB*[25,51], signaling to cognate receptors *TNFRSF12A* and *PDGFRA* on SAMes (Fig 6c). We confirmed localization of these ligand-receptor pairs within the fibrotic niche of human cirrhotic human liver (Fig. 6d, e). Both TNFSF12 and PDGF-BB induced primary human HSC proliferation, which was inhibited by blockade of TNFSF12A and PDGFRA respectively (Fig. 6f, g). Importantly, conditioned media from primary human SAM promoted primary human HSC proliferation *ex vivo* (Fig. 6h), demonstrating a functional role for SAM in regulating SAMes expansion.

SAEndo expressed high levels of non-canonical Notch ligands *JAG1*, *JAG2* and *DLL4* interacting with Notch receptor *NOTCH3* on SAMes (Fig. 6i). Primary endothelial cells from cirrhotic human liver demonstrated increased expression of JAG1 (Fig. 6j), whilst NOTCH3 was identified on PDGFRα^{+} SAMes within the fibrotic niche (Fig. 6k). Co-culture of primary human HSC and endothelial cells from cirrhotic livers promoted fibrillar collagen production by HSC, which was inhibited by addition of the Notch-signalling inhibitor Dibenzazepine (DBZ) (Fig. 6l, m). Furthermore, knockdown of *NOTCH3* expression in primary human HSC resulted in reduced fibrillar collagen expression (Fig. 6n), confirming that Notch-signalling promotes a fibrogenic mesenchymal cell phenotype[45].

SAMes expressed a number of ligands demonstrating statistically significant interactions with receptors on SAM and SAEndo (Extended Data Fig. 10b). In particular, SAMes expressed chemokines such as *CCL2,* which regulates monocyte-macrophage recruitment and phenotype (Extended Data Fig. 10c, d). Furthermore, immunoregulatory ligands such as *IL34, CSF1* and *CX3CL1* expressed by SAMes (Extended Data Fig. 10c) are known to modulate macrophage function, survival and proliferation[72,73], potentially explaining the increased proliferation rate observed in human SAM (Extended Data Fig. 4j, k). Intrahepatic angiogenesis is associated with both degree of liver fibrosis and portal hypertension, a major clinical consequence of liver cirrhosis[74]. Our fibrotic niche interactome analysis confirmed a number of pro-angiogenic interactions, with both SAMes (Extended Data Fig. 10c, d) and SAM (Extended Data Fig. 10e-g) expressing angiogenic ligands, with cognate receptors expressed by SAEndo. Additionally, SAEndo expressed *CSF1* and *CD200* (Extended Data Fig. 10h-j), suggestive of an immunomodulatory role. This is emphasized by the highly significant interactions detected between Notch ligand expression by SAEndo and *NOTCH2* expression by SAM (Extended Data Fig. 10i, j). Vascular Notch ligand expression regulates monocyte-derived macrophage differentiation and macrophage function in tissue repair[75], congruent with our data demonstrating upregulation of the transcription factor regulon for the Notch-target *HES1*, during differentiation from monocytes to SAM (Fig. 3h, Extended Data Fig. 5f, g). Hence, SAEndo are likely to regulate immune function as well as leucocyte recruitment to the fibrotic niche (Extended Data Fig. 8e).

In summary, our unbiased dissection of the key ligand-receptor interactions between novel scar-associated macrophages, endothelial and mesenchymal cells in the fibrotic niche, highlights TNFRSF12A, PDGFRA and Notch signaling as important regulators of mesenchymal cell function and hepatic fibrogenesis. Therapeutic targeting of these intra-scar pathways represents a rational approach for the discovery of novel antifibrotic treatments for patients with chronic liver disease.

Discussion

The fibrotic niche has not previously been defined in human liver. Here, using scRNA-seq and spatial mapping, we resolve the fibrotic niche of human liver cirrhosis, identifying novel pathogenic subpopulations of $TREM2^{+}CD9^{+}$ pro-fibrogenic macrophages, $ACKR1^{+}$ and $PLVAP^{+}$ endothelial cells and $PDGFR\alpha^{+}$ collagen-producing myofibroblasts. We dissect a complex, pro-fibrotic interactome between multiple novel scar-associated cells and identify highly relevant intra-scar pathways that are potentially druggable. This multi-lineage single cell dataset of human liver cirrhosis should serve as a useful resource for the scientific community, and is freely available for interactive browsing at http://www.livercellatlas.mvm.ed.ac.uk

Despite significant progress in our understanding of the molecular pathways driving liver fibrosis in rodent models, a lack of corollary studies in diseased human liver tissue has hindered translation into effective therapies, with currently no FDA or EMA-approved antifibrotic treatments available. Our multi-lineage ligand-receptor analysis demonstrates the complexity of interactions within the fibrotic niche, highlighting exemplar pathways such as TNFRSF12A, PDGFR and NOTCH signalling as key regulators of mesenchymal cell function in fibrotic human liver. These data provide a conceptual framework for more rational studies of antifibrotic therapies in both pre-clinical animal models and translational systems such as human liver organoid cultures[5,76,77]. Further, this unbiased multi-lineage approach should inform the design of combination therapies which will very likely be necessary to achieve effective antifibrotic potency[5,6].

Macrophages and endothelial cells are known to regulate liver fibrosis in rodent models[14,20,24,48,49]. However, little is known regarding the heterogeneity and precise molecular definitions of these cell types in human liver disease. Our data demonstrates

both the accumulation of discrete monocyte-derived macrophage and endothelial cell populations in the fibrotic niche of cirrhotic livers, but also the persistence of spatially distinct, non-scar associated resident Kupffer cells and liver sinusoidal endothelial cells. This single-cell approach has important implications for therapy development; facilitating targeting of pathogenic cells without perturbing homeostatic function.

In this era of precision medicine, where molecular profiling guides the development of highly targeted therapies, we used scRNA-seq to resolve the key non-parenchymal cell subclasses inhabiting the fibrotic niche of human liver cirrhosis. Application of our novel scar-associated cell markers could potentially inform molecular pathology-based patient stratification, which is fundamental to the prosecution of successful antifibrotic clinical trials. Our work illustrates the power of single-cell transcriptomics to decode the cellular and molecular basis of human organ fibrosis, providing a conceptual framework for the discovery of relevant and rational therapeutic targets to treat patients with a broad range of fibrotic diseases.

Note to referees:

http://www.livercellatlas.mvm.ed.ac.uk will be made freely available. For review purposes, log-in details are username: Edinburghlivercellatlas; password: Cirrhosis; please refresh your browser if the webpage does not load at first attempt.

Methods

Study subjects

Local approval for procuring human liver tissue and blood samples for scRNA-seq, flow cytometry and histological analysis was obtained from the NRS BioResource and Tissue Governance Unit (Study Number SR574), following review at the East of Scotland Research Ethics Service (Reference 15/ES/0094). All subjects provided written informed consent. Healthy background non-lesional liver tissue was obtained intraoperatively from patients undergoing surgical liver resection for solitary colorectal metastasis at the Hepatobiliary and Pancreatic Unit, Department of Clinical Surgery, Royal Infirmary of Edinburgh. Patients with a known history of chronic liver disease, abnormal liver function tests or those who had received systemic chemotherapy within the last four months were excluded from this cohort. Cirrhotic liver tissue was obtained intraoperatively from patients undergoing orthotopic liver transplantation at the Scottish Liver Transplant Unit, Royal Infirmary of Edinburgh. Blood from patients with a confirmed diagnosis of liver cirrhosis were obtained from patients attending the Scottish Liver Transplant Unit, Royal Infirmary of Edinburgh. Patients with liver cirrhosis due to viral hepatitis were excluded from the study. Patient demographics are summarised in Extended Data Fig. 1a. Isolation of primary hepatic macrophage subpopulations and endothelial cells from healthy and cirrhotic livers for cell culture and analysis of secreted mediators was performed at the University of Birmingham, UK. Local ethical approval was obtained (Reference 06/Q2708/11, 06/Q2702/61) and all patients provided written, informed consent. Liver tissue was acquired from explanted diseased livers from patients undergoing orthotopic liver transplantation, resected liver specimens or donor livers rejected for transplant at the Queen Elizabeth Hospital, Birmingham. For histological assessment of NAFLD biopsies, anonymised unstained formalin-fixed paraffin-embedded liver biopsy sections encompassing the complete NAFLD spectrum were provided by the Lothian NRS Human Annotated Bioresource under authority from the East of Scotland Research Ethics Service REC 1, reference 15/ES/0094.

Human tissue processing

For human liver scRNA-seq and flow cytometry analysis, a wedge biopsy of non-ischaemic fresh liver tissue (2-3 grams) was obtained by the operating surgeon, prior to interruption of the hepatic vascular inflow. This was immediately placed in HBSS (Gibco) on ice. The tissue was then transported directly to the laboratory and dissociation routinely commenced within 20 minutes of the liver biopsy. To enable paired histological assessment, a segment of each liver specimen was also fixed in 4% neutral-buffered formalin for 24 hours followed by paraffin-embedding. Additional liver samples, obtained via the same method, were fixed in an identical manner and used for further histological analysis. For human macrophage cell sorting and endothelial cell isolation, liver tissue (40 grams) was used from cirrhotic patients undergoing orthotopic liver transplantation or control samples from donor liver or liver resection specimens.

Animals

Adult male C57BL/6JCrl mice aged 8-10 weeks were purchased from Charles River. Mice were housed under specific pathogen-free conditions at the University of Edinburgh. All experiments were performed in accordance with UK Home Office regulations. Liver fibrosis was induced with 4 weeks (9 injections) of twice-weekly intraperitoneal carbon tetrachloride (CCl_4) at a dose of 0.4 µl/g body weight, diluted 1:3 in olive oil as previously described[15]. Liver tissue was harvested 24 hours following the final CCl_4 injection, a time of active fibrogenesis[15]. Comparison was made to age-matched uninjured mice.

Preparation of single-cell suspensions

For human liver scRNA-seq, liver tissue was minced with scissors and digested in 5mg/ml pronase (Sigma-Aldrich, P5147-5G), 2.93mg/ml collagenase B (Roche, 11088815001) and 1.9mg/ml DNase (Roche, 10104159001) at 37°C for 30 minutes with agitation (200–250 r.p.m.), then strained through a 120µm nybolt mesh along with PEB buffer (PBS, 0.1% BSA, and 2mM EDTA) including DNase (0.02mg/ml). Thereafter all processing was done at 4ºC. The cell suspension was centrifuged at 400*g* for 7 minutes, supernatant removed, cell pellet resuspended in PEB buffer and DNase added (0.02mg/ml), followed by additional centrifugation (400g, 7 minutes). Red blood

cell lysis was performed (BioLegend, 420301), followed by centrifugation (400*g*, 7 minutes), resuspension in PEB buffer and straining through a 35µm filter. Following another centrifugation at 400*g* for 7 minutes, cells were blocked in 10% human serum (Sigma-Aldrich, H4522) for 10 minutes at 4ºC prior to antibody staining.

For both human liver macrophage flow cytometry analysis and cell sorting and mouse liver macrophage flow cytometry, cell sorting and scRNA-seq, single-cell suspensions were prepared as previously described, with minor modifications[78]. In brief, liver tissue was minced and digested in an enzyme cocktail 0.625 mg/ml collagenase D (Roche, 11088882001), 0.85 mg/ml collagenase V (Sigma-Aldrich, C9263-1G), 1 mg/ml dispase (Gibco, Invitrogen, 17105-041), and 30 U/ml DNase (Roche, 10104159001) in RPMI-1640 at 37°C for 20 minutes (mouse) or 45 minutes (human) with agitation (200–250 r.p.m.), before being passed through a 100µm filter. Following red blood cell lysis (BioLegend, 420301), cells were washed in PEB buffer and passed through a 35µm filter. Before the addition of antibodies, cells from human samples were blocked in 10% human serum (Sigma-Aldrich, H4522) and mouse samples were blocked in anti-mouse CD16/32 antibody (1:100; Biolegend, 101302) and 10% normal mouse serum (Sigma, M5905) for 10 minutes at 4 °C.

For human PBMC scRNA-seq, 4.9ml peripheral venous blood samples were collected in EDTA-coated tubes (Sarstedt, S-Monovette® 4.9ml K3E) and placed on ice. Blood samples were transferred into a 50ml Falcon tube. Following red cell lysis (Biolegend, 420301), blood samples were then centrifuged at 500g for 5 minutes and supernatant was removed. Pelleted samples were then resuspended in staining buffer (PBS plus 2% BSA; Sigma-Aldrich) and centrifugation was repeated. Samples were then blocked in 10% human serum (Sigma-Aldrich, H4522) in staining buffer on ice for 30 minutes. Cells were then resuspended in staining buffer and passed through a 35µm filter prior to antibody staining.

Flow cytometry and cell sorting

Incubation with primary antibodies was performed for 20 minutes at 4°C. All antibodies, conjugates, lot numbers and dilutions used in this study are presented in Supplementary Table 18. Following antibody staining, cells were washed with PEB

buffer. For both human macrophage flow cytometry analysis and cell sorting, cells were then incubated with streptavidin-BV711 for 20 minutes at 4°C (Biolegend 405241; Dilution 1:200). For human and mouse cell sorting (FACS) and mouse flow cytometry analysis, cell viability staining (DAPI; 1:1000 dilution) was then performed, immediately prior to acquiring the samples.

Human cell sorting for scRNA-seq was performed on a BD Influx (Becton Dickinson, Basel, Switzerland). Viable single $CD45^+$ (leucocytes) or $CD45^-$ (other non-parenchymal cells) cells were sorted from human liver tissue (Extended Data Fig. 1b) and viable $CD45^+$ $CD66b^-$ (PBMC) cells were sorted from peripheral blood (Extended Data Fig. 1c) and processed for droplet-based scRNA-seq.

To generate conditioned media from cirrhotic liver macrophage subpopulations, cells were sorted on a BD FACSAria™ Fusion (Becton Dickinson, Basel, Switzerland). Sorted SAM (viable $CD45^+Lin^-HLA\text{-}DR^+CD14^+CD16^+CD163^-TREM2^+CD9^+$), TMo (viable $CD45^+Lin^-$ $HLA\text{-}DR^+CD14^+CD16^+CD163^-TREM2^-CD9^-$) and KC (viable $CD45^+Lin^-$ $HLA\text{-}DR^+CD14^+CD16^+CD163^+CD9^-$) were plated in 12-well plates (Corning, 3513) in DMEM (Gibco, 41965039) containing 2% FBS (Gibco, 10500056) at $1x10^6$ cells/ml for 24 hours at 37°C 5%CO_2. Control wells contained media alone. Conditioned media was collected, centrifuged at 400g for 10 minutes and supernatant stored at -80°C.

For human macrophage flow cytometry analysis, following surface antibody staining, cells were stained with Zombie NIR fixable viability dye (Biolegend, 423105) according to manufacturers' instructions. Cells were washed in PEB then fixed in IC fixation buffer (Thermo-Fisher, 00-8222-49) for 20 minutes at 4°C. Fixed samples were stored in PEB at 4°C until acquisition. Flow cytometry acquisition was performed on 6-laser Fortessa flow cytometer (Becton Dickinson, Basel, Switzerland). The gating strategy is shown (Extended Data Fig. 4f, Fig. 2f).

Mouse macrophage cell sorting for scRNA-seq and co-culture experiments was performed on a BD FACSAriaII (Becton Dickinson, Basel, Switzerland). For scRNA-seq, viable $CD45^+$ $Lin(CD3, NK1.1, Ly6G, CD19)^-$ cells were sorted from healthy (n=3) and CCl_4-treated (n=3) mice and processed for droplet-based scRNA-seq. For

transwell co-culture, viable $CD45^+$ Lin^- $CD11b^+$ $F4/80^+$ $TIMD4^-$ $CD9^+$ (mSAM) or $CD9^-$ (mTMo) cells were sorted from CCl_4-treated mice (Extended Data Fig. 6e). Flow cytometry analysis on macrophages from healthy and CCl_4-treated mice was also performed on a BD FACSAriaII (Becton Dickinson, Basel, Switzerland), using the same gating strategy (Extended Data Fig. 6e). All flow cytometry data was analysed using Flowjo software (Treestar, Ashland, TN).

Luminex Assay

Detection of CCL2, Galectin-3, IL-1 beta, CXCL8 and Osteopontin (SPP1) proteins in conditioned media from human liver macrophage subpopulations was performed using a custom human luminex assay (R&D systems), according to the manufacturers protocol. Data was acquired using a Bio-Plex® 200 (Bio-Rad, UK) and is presented a median fluorescence intensity (MFI) for each analyte.

Cell Culture

Human hepatic stellate cell activation

Primary human hepatic stellate cells (HSC) were purchased (ScienCell, 5300) and cultured in stellate cell medium (SteCM, ScienCell, 5301) on Poly-L-Lysine (Sigma, P4832) coated T75 tissue culture flasks, according to the suppliers protocol. All experiments were performed using cells between passage 3 and 5. For assessment of fibrillar collagen gene expression, HSC were plated at 75,000 cells per well in 24 well-plates (Costar, 3524) in HSC media consisting of DMEM (Gibco, 21969-035) supplemented with 20 µM HEPES (Sigma, H3375,), 2 mM L-Glutamine (Gibco , 25030-024), 1% Penicillin Streptomycin (Gibco, 15140-122, Gibco) and 2% Foetal Bovine Serum (FBS, Gibco, 10270). HSC were serum starved overnight (in HSC media without FBS), washed with PBS, then 250µl of conditioned media from primary human macrophage subpopulations added for 24 hours. HSC were harvested for RNA.

Human hepatic stellate cell proliferation

For proliferation assays, following serum starvation HSC were harvested using TrypLE Express (Gibco, Cat. no. 12604013), re-suspended in HSC media at $2.5x10^4$/ml with Incucyte NucLight Rapid Red (Essen Biosciences, 4717) at a dilution of 1 in 500 and

seeded into 384 well plates (Greiner Bio-One, 781090) at 25µl per well. HSC were then treated with control media or (i) PDGF-BB (10ng/ml; Peprotech, 100-14B) or TNFSF12 (100ng/ml; Peprotech, 310-06-5) with or without the PDGFRα inhibitor Crenolanib[79] (1µM; Cayman chemicals, CAY1873), anti-TNRSF12A (2µg/ml; Life Technologies, 16-9018-82, clone ITEM-4), mouse IgG2b kappa isotype control antibody (2µg/ml; Life Technologies, 16-4732-82, clone eBMG2b) or vehicle control as indicated or (ii) conditioned media from human hepatic macrophage subpopulations as indicated. The final volume was 50µl for all conditions. Cells were then incubated in an Incucyte ZOOM live cell analysis system (Essen Biosciences) humidified at 37°C with 5% CO_2 with imaging every 3 hours using the 10x optic for either 87 hours (recombinant cytokines/inhibitors) or 39 hours (macrophage conditioned media). Analysis was performed with the Incucyte proprietary analysis software (version 2018A) by using machine learning to distinguish the individual nuclei (stained red by the NucLight Rapid Red dye) and perform nuclear counts of the images at each 3 hour time point over the period of culture. Data are expressed as area under curve (AUC) for % change in nuclear number from baseline *versus* time (hours), calculated in GraphPad Prism (GraphPad Software, USA).

Gene knockdown in human hepatic stellate cells

Knockdown of NOTCH3 in human HSC was performed using siRNA. HSC were plated at 75,000 cells per well in a 12 well plate (Costar, 3513) followed by serum starvation overnight (in HSC medium without FBS). siRNA duplexes with Lipofectamine RNAiMAX Transfection Reagent (ThermoFisher, 13778075) were prepared in OptiMEM (ThermoFisher, 31985070) according to the manufacturer's recommendations, and used at a concentration of 50nM. Cells were exposed to the duplex for 48 hours, in HSC media containing 2% FBS. Cells were harvested for RNA and RT-qPCR. Knockdown efficiency was assessed by NOTCH3 RT-qPCR. The best siRNA for knockdown was determined empirically using the FlexiTube GeneSolution kit (Qiagen, GS4854). HSC treated with control siRNA (Qiagen, 1027280) and siRNA for NOTCH3 (Qiagen, Hs_NOTCH3_3, SI00009513; knockdown 83%) were then assessed for fibrillar collagen gene expression.

Mouse hepatic stellate cell activation

Primary murine HSC culture were isolated from healthy mice as described[80]. Briefly, after cannulation of the inferior vena cava, the portal vein was cut to allow retrograde step-wise perfusion with pronase (Sigma, P5147) and collagenase D (Roche, 11088882001) containing solutions, before *ex vivo* digestion in a solution containing pronase, collagenase D and Dnase1 (Roche, 10104159001). HSC were isolated from the digest solution by Histodenz (Sigma, D2158-100G) gradient centrifugation. HSC were plated at a density of 400,000 cells per well in a 24 well plate (Costar, 3524) in HSC media containing 10% FBS. Following overnight culture, cells were washed with PBS and cultured in HSC media containing 2% FBS. For macrophage co-culture, transwell inserts (0.4µm polyester membrane; Costar, 3470) were then placed above adherent HSC. FACS-sorted $CD9^+$ mSAM or $CD9^-$ mTMo from CCl_4-treated mice were resuspended in HSC media containing 2% FBS at 400,000 cells/ml and 200,000 cells added to the top of the transwell insert. Co-culture proceeded for 48 hours and HSC were harvested for RNA. Quiescent HSC (harvested at start of co-culture) were used as a control population.

Human liver endothelial cell isolation

Human liver endothelial cells (LEC) were isolated from cirrhotic explant livers and non-fibrotic control donor liver as previously described[81]. Endothelial cells were cultured on plasticware coated with rat-tail collagen (Sigma, C3867) in complete LEC medium consisting of endothelial basal media (ThermoFisher, 11111044) containing 10% heat inactivated human serum (tcsBiosciences, CS100-500), 100U penicillin, 100 µg/mL streptomycin, 2mM glutamine (Sigma, G6784), VEGF (10 ng/mL; Peprotech, 100-20) and 10 ng/mL HGF (10 ng/mL; Peprotech, 100-39). LEC expression of PLVAP, CD34, ACKR1 and JAG1 was assessed using flow cytometry.

Flow-based adhesion assays

Flow-based adhesion assays were performed as described[56,81]. Briefly, LEC from healthy and cirrhotic liver were seeded into a rat-tail collagen coated Ibidi slide $VI^{0.4}$ (Ibidi, 80606) at a density to give a monolayer and incubated overnight. Peripheral blood was collected from healthy donors in EDTA-coated tubes. Peripheral blood monocuclear cells (PBMC) were isolated using a lympholyte density gradient (Cedarlane laboratories) then washed in PBS containing 1mM Ca^{2+}, 0.5 mM Mg^{2+} and

0.15% bovine serum albumin (PBS/BSA). Monocytes were enriched from PBMC using pan-monocyte isolation kit (Miltenyi biotech, 130-096-537) according the manufacturer's protocol. For flow-based adhesion assay, cells were resuspended at 10^6 cells per millilitre in endothelial basal media (ThermoFisher, 11111044) containing 0.15% BSA, then perfused over the LEC monolayer for 5min at 0.28ml/min. Non-adherent cells were washed off during 5min perfusion of 0.15% BSA human basal endothelial medium and 10 random non-overlapping images were randomly recorded from each channel. Total adherent (bright-phase; expressed as cell number/mm^2/1 million cells perfused) and transmigrating cells (dark-phase; expressed as percentage total adherent cells) on an LEC monolayer from each patient were counted and quantified as previously described[56].

Gene knockdown in endothelial cells

Knockdown of ACKR1 and PLVAP gene expression in human cirrhotic LEC was performed using siRNA as previously described[81]. In brief, siRNA duplexes for PLVAP, ACKR1, or negative control (Qiagen, 1027280) with Lipofectamine RNAiMAX Transfection Reagent (ThermoFisher, 13778075) were prepared in OptiMEM (ThermoFisher, 31985070) according to the manufacturer's recommendations, and used at a concentration of 25nM. Cells were exposed to the duplex for 4 hours at 37°C after which time the media was replaced with endothelial basal media containing 10% heat-inactivated human serum for 24 hours. The media was then replaced with complete LEC media and incubated at 37°C with 5% CO_2 for a further 24 hours. Knockdown efficacy was assessed by flow cytometry and mean fluorescence intensity (Extended Data Fig. 8f). The best siRNA for knockdown was determined empirically using the FlexiTube GeneSolution kit (Qiagen, GS83483 (PLVAP) and GS2532 (ACKR1)). For flow-based adhesion assays, siRNAs for PLVAP (Qiagen, Hs_PLVAP_1, SI00687547; knockdown 50.6%, ACKR1 (Qiagen, Hs_Fy_5, SI02627667; knockdown 37.7%) or control siRNA were selected. 90,000 LEC from cirrhotic patients (n=6) were seeded into channels of a rat-tail collagen coated Ibidi slide $VI^{0.4}$, gene knockdown performed, followed by flow-based adhesion assay as described above.

Endothelial and hepatic stellate cell co-culture

HSC (15,000 cells) were seeded into an Ibidi slide VI$^{0.4}$ with and without primary human LEC (15,000 cells) from individual cirrhotic patients (n=3) in LEC complete medium. After 2h, all growth factor supplements were removed and cells were cultured for a further 72 hours in endothelial basal media containing 10% heat-inactivated human serum ± Notch-signalling inhibitor Dibenzazepine (Bio-Techne, 4489/10) or vehicle (DMSO) control. Cells were fixed in 4% PFA for 30 minutes, permeabilised with 0.3% Triton PBS for 5 minutes, blocked with 10% goat serum in PBS for 30 minutes followed by primary antibody incubation (mouse anti-PECAM1 and rabbit anti-collagen 1; see Supplementary table 18) for 1 hour. Cells were washed in 0.1% Triton PBS followed by addition of fluorescently-conjugated secondary antibodies (1:500 dilution) for 1 hour. Cells were mounted with Pro-long Gold anti-fade DAPI, images were taken on the Confocal Microscope Zeiss LSM780, and collagen 1 area staining quantified using IMARIS.

RNA extraction and RT-qPCR

RNA was isolated from HSC using the RNeasy Plus Micro Kit (Qiagen, 74034) and cDNA synthesis performed using QuantiTect Reverse Transcription Kit (Qiagen, 205313) according to the manufacturer's protocol. Reactions were performed in triplicate in 384-well plate format and were assembled using the QIAgility automated pipetting system (Qiagen). RT-qPCR for human HSC was performed using PowerUp SYBR Green Master Mix (ThermoFisher, A25777) with the following primers (all Qiagen): *GAPDH* (QT00079247), *COL1A1* (QT00037793), *COL3A1* (QT00058233), *NOTCH3* (QT00003374). RT-qPCR for mouse HSC was performed using TaqMan Fast Advanced Master Mix (ThermoFisher, 4444557) with the following primers: *Gapdh* (ThermoFisher, Mm99999915_g1) and *Col3a1* (ThermoFisher, Mm00802300_m1). Samples were amplified on an ABI 7900HT FAST PCR system (Applied Biosystems, ThermoFisher Scientific). Data was analysed using ThermoFisher Connect cloud qPCR analysis software (ThermoFisher Scientific). The $2^{-\Delta\Delta Ct}$ quantification method, using *GAPDH* for normalization, was used to estimate the amount of target mRNA in samples, and expression calculated relative to average mRNA expression levels from control samples.

Immunohistochemistry, immunofluorescence, smFISH

Formalin-fixed paraffin-embedded human liver tissue was cut into 4 μm sections, dewaxed, rehydrated, then incubated in 4% neutral-buffered formalin for 20 minutes. Following heat-mediated antigen retrieval in pH6 sodium citrate (microwave; 15 minutes), slides were washed in PBS and incubated in 4% hydrogen peroxide for 10 minutes. Slides were then washed in PBS, blocked using protein block (GeneTex, GTX30963) for 1 hour at room temperature before incubation with primary antibodies for 1 hour at room temperature. A full list of primary antibodies and conditions are shown in Supplementary Table 18. Slides were washed in PBST (PBS plus 0.1% Tween20; Sigma-Aldrich, P1379) then incubated with ImmPress HRP Polymer Detection Reagents (depending on species of primary; rabbit, MP-7401; mouse, MP-6402-15; goat, MP-7405; all Vector Laboratories) for 30 minutes at room temperature. Slides were washed in PBS followed by detection. For DAB staining, sections were incubated with DAB (DAKO, K3468) for 5 minutes and washed in PBS before a haematoxylin (Vector Laboratories, H3404) counterstain. For multiplex immunofluorescence staining, following the incubation with ImmPress and PBS wash, initial staining was detected using either Cy3, Cy5, or Fluorescein tyramide (Perkin-Elmer, NEL741B001KT) at a 1:1000 dilution. Slides were then washed in PBST followed by further heat treatment with pH6 sodium citrate (15 minutes), washes in PBS, protein block, incubation with the second primary antibody (incubated overnight at 4°C), ImmPress Polymer and tyramide as before. This sequence was repeated for the third primary antibody (incubated at room temperature for 1 hour) and a DAPI-containing mountant was then applied (ThermoFisher Scientific, P36931). All immunofluorescence stains were repeated in a minimum of 3 patients and representative images are displayed.

For AMEC Staining (only CLEC4M immunohistochemistry), all washes were carried out with TBST (dH_2O, 2oomM Tris, 1.5M NaCl, 1% Tween20 (all Sigma-Aldrich) pH7.5) and peroxidase blocking was carried out for 30mins in 0.6% hydrogen peroxide in Methanol. Sections were incubated with AMEC (Vector Laboratories, SK-4285) for 20 minutes and washed in TBST (dH_2O, 200mM Tris, 1.5M NaCl, 1% Tween20 (all Sigma-Aldrich)) before a haematoxylin (Vector Laboratories, SK-4285) counterstain.

For combined single-molecule fluorescent in situ hybridization (smFISH) and immunofluorescence, detection of TREM2 was performed using the RNAscope® 2.5 LS Reagent Kit - BrownAssay (Advanced Cell Diagnostics (ACD)) in accordance with the manufacturer's instructions. Briefly, 5 µm tissue sections were dewaxed, incubated with endogenous enzyme block, boiled in pretreatment buffer and treated with protease, followed by target probe hybridization using the RNAscope® LS 2.5 Hs-TREM2 (420498, ACD) probe. Target RNA was then detected with Cy3 tyramide (Perkin-Elmer, NEL744B001KT) at 1:1000 dilution. The sections were then processed through a pH6 sodium citrate heat-mediated antigen retrieval, hydrogen peroxidase treatment and protein block (all as for multiplex immunofluorescence staining as above). MNDA antibody was applied overnight at 4°C, completed using a secondary ImmPress HRP Anti-Rabbit Peroxidase IgG (Vector Laboratories, MP7401), visualised using a Flourescein tyramide (Perkin-Elmer, NEL741B001KT) at a 1:1000 dilution and stained with DAPI.

Brightfield and fluorescently-stained sections were imaged using the slide scanner AxioScan.Z1 (Zeiss) at 20X magnification (40X magnification for smFISH). Images were processed and scale bars added using Zen Blue (Zeiss) and Fiji software[82].

Cell counting and image analysis

Automated cell counting was performed using QuPath software[83]. Briefly, DAB-stained whole tissue section slide-scanned images (CZI files) were imported into QuPath. Cell counts were carried out using the positive cell detection tool, detecting haematoxylin-stained nuclei and then thresholding for positively-stained DAB cells, generating DAB-positive cell counts/mm^2 tissue. Identical settings and thresholds were applied to all slides for a given stain and experiment. For cell counts of fibrotic septae vs parenchymal nodules, the QuPath segmentation tool was used to segment the DAB-stained whole tissue section into fibrotic septae or non-fibrotic parenchymal nodule regions using tissue morphological characteristics (Fig. 2j). Positive cell detection was then applied to the fibrotic and non-fibrotic regions in turn, providing cell DAB-positive cell counts/mm^2 in fibrotic septae and non-fibrotic parenchymal nodules for each tissue section.

Digital morphometric pixel analysis was performed using the Trainable Weka Segmentation (TWS) plugin[84] in Fiji software[82]. Briefly, each stained whole tissue section slide-scanned image was converted into multiple TIFF files in Zen Blue software (Zeiss). TIFF files were imported into Fiji and TWS plugin trained to produce a classifier which segments images into areas of positive staining, tissue background and white space[84]. The same trained classifier was then applied to all TIFF images from every tissue section for a particular stain, providing a percentage area of positive staining for each tissue section. For digital morphometric quantification of positive staining of fibrotic septae *versus* parenchymal nodules, TIFF images were segmented into fibrotic septae or non-fibrotic parenchymal nodule regions using tissue morphological characteristics, followed by analysis using the TWS plugin in Fiji software.

Histological assessment of NASH sections

Haematoxylin and eosin and picro-sirius red stained sections from each case were whole-slide imaged using a NanoZoomer imager (Hamamatsu Photonics, Japan). Images of stained sections were independently scored by a consultant liver transplant histopathologist (T.J.K.) at the national liver transplant centre with experience in trial scoring by applying the ordinal NAFLD activity score[85]. For observer-independent quantification of picro-sirius red positive staining, images were split using ndpisplit[86] into tiles of x5 magnification before the application of a classifier that had been trained by the liver histopathologist using the machine learning WEKA plugin in FIJI[82,84], as previously described[87]. All analysis was undertaken blind to all other data.

Droplet-based scRNA-seq

Single cells were processed through the Chromium™ Single Cell Platform using the Chromium™ Single Cell 3' Library and Gel Bead Kit v2 (10X Genomics, PN-120237) and the Chromium™ Single Cell A Chip Kit (10X Genomics, PN-120236) as per the manufacturer's protocol. In brief, single cells were sorted into PBS + 0.1% BSA, washed twice and counted using a Bio-Rad TC20. 10,769 cells were added to each lane of the 10X chip. The cells were then partitioned into Gel Beads in Emulsion in the

Chromium™ instrument, where cell lysis and barcoded reverse transcription of RNA occurred, followed by amplification, fragmentation and 5′ adaptor and sample index attachment. Libraries were sequenced on an Illumina HiSeq 4000.

Computational Analysis

Pre-processing scRNA-seq data

We aligned to the GRCh38 and mm10 (Ensembl 84) reference genomes as appropriate for the input dataset, and estimated cell-containing partitions and associated UMIs, using the Cell Ranger v2.1.0 Single-Cell Software Suite from 10X Genomics. Genes expressed in fewer than three cells in a sample were excluded, as were cells that expressed fewer than 300 genes or mitochondrial gene content >30% of the total UMI count. We normalised by dividing the UMI count per gene by the total UMI count in the corresponding cell and log-transforming. Variation in UMI counts between cells was regressed according to a negative binomial model, prior to scaling and centering the resulting value by subtracting the mean expression of each gene and dividing by its standard deviation (E_n), then calculating $\ln(10^4 * E_n + 1)$.

Dimensionality reduction, clustering, and DE analysis

We performed unsupervised clustering and differential gene expression analyses in the *Seurat* R package v2.3.0[88]. In particular we used SNN graph-based clustering, where the SNN graph was constructed using from 2 to 11 principal components as determined by dataset variability shown in principal components analysis (PCA); the resolution parameter to determine the resulting number of clusters was also tuned accordingly. To assess cluster similarity we used the *BuildClusterTree* function from *Seurat*.

In total, we present scRNA-seq data from ten human liver samples (named Healthy 1-5 and Cirrhotic 1-5), five human blood samples (n=4 cirrhotic named Blood 1-4 and n=1 healthy named PBMC8K; pbmc8k dataset sourced from single-cell gene expression datasets hosted by 10X Genomics), and two mouse liver samples (n=3 uninjured and n=3 fibrotic). For seven human liver samples (Healthy 1-4 and Cirrhotic 1-3) we performed scRNA-seq on both leucocytes ($CD45^+$) and other non-parenchymal cells ($CD45^-$); for the remaining three human livers (Healthy 5, Cirrhotic 4-5) we performed scRNA-seq on leucocytes only (Extended Data Fig. 2e, g).

Initially, we combined all human scRNA-seq datasets (liver and blood) and performed clustering analysis with the aim of isolating a population of liver-resident cells, by identifying contaminating circulatory cells within datasets generated from liver digests and removing them from downstream analysis. Specifically, we removed from our liver datasets cells that fell into clusters 1 and 13 of the initial dataset in Extended Data Fig. 1d.

Using further clustering followed by signature analysis, we interrogated this post-processed liver-resident cell dataset for robust cell lineages. These lineages were isolated into individual datasets, and the process was iterated to identify robust lineage subpopulations. At each stage of this process we removed clusters expressing more than one unique lineage signature in more than 25% of their cells from the dataset as probable doublets. Where the cell proliferation signature identified distinct cycling subpopulations, we re-clustered these again to ascertain the identity of their constituent cells.

The murine scRNA-seq datasets were combined, clustered, and interrogated for cell lineages in a similar manner as their human counterparts.

All heatmaps, t-SNE and UMAP visualisations, violin plots, and dot plots were produced using *Seurat* functions in conjunction with the *ggplot2*, *pheatmap*, and *grid* R packages. t-SNE and UMAP visualisations were constructed using the same number of principal components as the associated clustering, with perplexity ranging from 30 to 300 according to the number of cells in the dataset or lineage. We conducted differential gene expression analysis in *Seurat* using the standard AUC classifier to assess significance. We retained only those genes with a log-fold change of at least 0.25 and expression in at least 25% of cells in the cluster under comparison.

Defining cell lineage signatures

For each cell we obtained a signature score across a curated list of known marker genes per cell lineage in the liver (Supplementary Table 1). This signature score was defined as the geometric mean of the expression of the associated signature genes in that cell. Lineage signature scores were scaled from 0 to 1 across the dataset, and the score for

each cell with signature less than a given threshold (the mean of said signature score across the entire dataset) was set as 0.

Batch effect and quality control

To investigate agreement between samples we extracted the average expression profile for a given cell lineage in each sample, and calculated the Pearson correlation coefficients between all possible pairwise comparisons of samples per lineage[89].

Imputing dropout in T cell and ILC clusters

To impute dropout of low-abundance transcripts in our T cell and ILC clusters so that we might associate them with known subpopulations, we down-sampled to 7,380 cells from 36,900 and applied the *scImpute* R package v0.0.8[90], using as input both our previous annotation labels and k-means spectral clustering (k=5), but otherwise default parameters.

Analysing functional phenotypes of scar-associated cells

For further analysis of function we adopted the self-organising maps (SOM) approach as implemented in the *SCRAT* R package v1.0.0[91]. For each lineage of interest we constructed a SOM in *SCRAT* using default input parameters and according to its clusters. We defined the signatures expressed in a cell by applying a threshold criterion ($e^{thresh} = 0.95 \times e^{max}$) selecting the highest-expressed metagenes in each cell, and identified for further analysis those metagene signatures defining at least 30% of cells in at least one cluster within the lineage. We smoothed these SOMs using the *disaggregate* function from the *raster* R package for visualisation purposes, and scaled radar plots to maximum proportional expression of the signature. Gene ontology enrichment analysis on the genes in these spots was performed using PANTHER 13.1 (pantherdb.org).

Inferring injury dynamics and transcriptional regulation

To generate cellular trajectories (pseudotemporal dynamics) we used the *monocle* R package v2.6.1[92]. We ordered cells in a semi-supervised manner based on their *Seurat* clustering, scaled the resulting pseudotime values from 0 to 1, and mapped them onto either the t-SNE or UMAP visualisations generated by *Seurat* or diffusion maps as implemented in the *scater* R package v1.4.0[93] using the top 500 variable genes as input.

We removed mitochondrial and ribosomal genes from the geneset for the purposes of trajectory analysis. Differentially-expressed genes along this trajectory were identified using generalised linear models via the *differentialGeneTest* function in *monocle*.

When determining significance for differential gene expression along the trajectory, we set a q-value threshold of $1e^{-20}$. We clustered these genes using hierarchical clustering in *pheatmap*, cutting the tree at k=3 to obtain gene modules with correlated gene expression across pseudotime. Cubic smoothing spline curves were fitted to scaled gene expression along this trajectory using the *smooth.spline* command from the *stats* R package, and gene ontology enrichment analysis again performed using PANTHER 13.1.

We verified the trajectory and its directionality using the *velocyto* R package v0.6.0[34], estimating cell velocities from their spliced and unspliced mRNA content. We generated annotated spliced and unspliced reads from the 10X BAM files via the *dropEst* pipeline, before calculating gene-relative velocity using kNN pooling with k=25, determining slope gamma with the entire range of cellular expression, and fitting gene offsets using spanning reads. Aggregate velocity fields (using Gaussian smoothing on a regular grid) and transition probabilities per lineage subpopulations were visualised on t-SNE, UMAP, or diffusion map visualisations as generated previously. Gene-specific phase portraits were plotted by calculating spliced and unspliced mRNA levels against steady-state inferred by a linear model; levels of unspliced mRNA above and below this steady-state indicate increasing and decreasing expression of said gene, respectively. Similarly we plotted unspliced count signal residual per gene, based on the estimated gamma fit, with positive and negative residuals indicating expected upregulation and downregulation respectively.

For transcription factor analysis, we obtained a list of all genes identified as acting as transcription factors in humans from AnimalTFDB[94]. To further analyse transcription factor regulons, we adopted the *SCENIC* v0.1.7 workflow in R[95], using default parameters and the normalised data matrices from *Seurat* as input. For visualisation, we mapped the regulon activity (AUC) scores thus generated to the pseudotemporal trajectories from *monocle* and the clustering subpopulations from *Seurat*.

Analysing inter-lineage interactions within the fibrotic niche

For comprehensive systematic analysis of inter-lineage interactions within the fibrotic niche we used CellPhoneDB[69]. CellPhoneDB is a manually curated repository of ligands, receptors, and their interactions, integrated with a statistical framework for inferring cell-cell communication networks from single-cell transcriptomic data. In brief, we derived potential ligand-receptor interactions based on expression of a receptor by one lineage subpopulation and a ligand by another; as input to this algorithm we used cells from the fibrotic niche as well as liver sinusoidal endothelial cells and Kupffer cells as control, and we considered only ligands and receptors expressed in greater than 5% of the cells in any given subpopulation. Subpopulation-specific interactions were identified as follows: 1) randomly permuting the cluster labels of all cells 1000 times and determining the mean of the average receptor expression of a subpopulation and the average ligand expression of the interacting subpopulation, thus generating a null distribution for each ligand-receptor pair in each pairwise comparison between subpopulations, 2) calculating the proportion of these means that were "as or more extreme" than the actual mean, thus obtaining a p-value for the likelihood of subpopulation specificity for a given ligand-receptor pair, 3) prioritising interactions that displayed specificity to subpopulations interacting within the fibrotic niche.

Canonical correlation analysis

To compare human and murine populations of monocytic phagocytes, we used canonical correlation analysis as implemented in *Seurat*[39]. We map the genes in the human dataset to their murine orthologues using *biomaRt*, discarding any genes for which no orthologues can be found. We then calculate the shared low-dimensional subspace on the union of genes that are variably expressed in both datasets (n=159), and align using six canonical components as determined by evaluating the biweight midcorrelation. Results are visualised on t-SNEs as previously described.

Deconvolution of whole liver microarray data

To assess macrophage composition early-stage NAFLD, we performed deconvolution analysis on publicly available microarray data from annotated liver biopsy specimens taken across the NAFLD disease spectrum (GEO accession GSE48452)[47]. Tissue MP cells from our human scRNA-seq data were manually clustered into the main annotated

MP populations. Signature gene expression profiles of SAM, TMo, KC were used to deconvolve the monocyte-macrophage composition of liver biopsy samples from GSE48452 using Cibersort[96], as previously described[46]. The monocyte-macrophage composition of each biopsy sample was then compared to the associated histological and demographic features, available from the GEO database.

Statistical Analysis

To assess whether our identified subpopulations were significantly overexpressed in injury, we posited the proportion of injured cells in each cluster as a random count variable using a Poisson process, as previously described[89]. We modelled the rate of detection using the total number of cells in the lineage profiled in a given sample as an offset, with the condition of each sample (healthy vs cirrhotic) provided as a covariate factor. The model was fitted using the R command *glm* from the *stats* package. The p-value for the significance of the proportion of injured cells was assessed using a Wald test on the regression coefficient. This methodology was also applied to assess significant changes in proportions of mononuclear phagocytes between healthy and cirrhotic liver tissue by flow cytometry.

Remaining statistical analyses were performed using GraphPad Prism (GraphPad Software, USA). Comparison of changes between two groups was performed using a Mann-Whitney test (unpaired; two-tailed) or using a Wilcoxon matched-pairs signed rank test (paired; two-tailed). Comparison of changes between multiple groups was performed using a Kruskal-Wallis and Dunn, one-way ANOVA and Tukey or repeated measures one-way ANOVA and Tukey tests. Correlations were preformed using Pearson correlation and best fit line plotted using linear regression. P-values<0.05 were considered statistically significant.

Data and materials availability

Our expression data will be freely available for user-friendly interactive browsing online at http://www.livercellatlas.mvm.ed.ac.uk (log-in details for purposes of review; username: Edinburghlivercellatlas; password: Cirrhosis). CellPhoneDB is available at www.CellPhoneDB.org, along with lists of membrane proteins, ligands and receptors,

and heteromeric complexes. All raw sequencing data will be deposited in the Gene Expression Omnibus (GEO; GEO NO. XXXX).

Code availability

R scripts enabling the main steps of the analysis are available from the corresponding authors on reasonable request.

Acknowledgements

This work was supported by an MRC Clinician Scientist Fellowship (MR/N008340/1) to P.R., a Wellcome Trust Senior Research Fellowship in Clinical Science (ref. 103749) to N.C.H., an AbbVie Future Therapeutics and Technologies Division grant to N.C.H., a CORE – Children's Liver Disease Foundation grant (ref. R43927) to N.C.H. and a Tenovus Scotland grant (ref. E18/05) to R.D. and N.C.H. R.V-T. was funded by EMBO and Human Frontiers long-term fellowships. C.J.W. was funded by a BBSRC New Investigator Award (BB/N018869/1). P.N.N., C.J.W. and N.T.L. are funded by the NIHR Birmingham Biomedical Research Centre at the University Hospitals Birmingham NHS Foundation Trust and the University of Birmingham. This paper presents independent research supported by the NIHR Birmingham Biomedical Research Centre at the University Hospitals Birmingham NHS Foundation Trust and the University of Birmingham. The views expressed are those of the author(s) and not necessarily those of the NHS, the NIHR or the Department of Health and Social Care. J.P.I. is funded by the NIHR Bristol Biomedical Research Centre, University Hospitals Bristol Foundation Trust and the University of Bristol. We thank the patients who donated liver tissue and blood for this study. We thank J. Davidson, C. Ibbotson, J. Black and A. Baird of the Scottish Liver Transplant Unit and the research nurses of the Wellcome Trust Clinical Research Facility for assistance with consenting patients for this study. We thank the liver transplant coordinators and surgeons of the Scottish Liver Transplant Unit and the surgeons and staff of the Hepatobiliary Surgical Unit, Royal Infirmary of Edinburgh for assistance in procuring human liver samples. We thank S. Johnston, W. Ramsay and M. Pattison (QMRI Flow Cytometry and Cell Sorting Facility, University of Edinburgh) for technical assistance with fluorescence activated cell sorting (FACS) and flow cytometry. We thank Jon Henderson for technical support and Gillian Muirhead for assistance with liver endothelial cell isolation.

Author Contributions

P.R. performed experimental design, tissue procurement, data generation, data analysis and interpretation, and manuscript preparation; R.D. performed experimental design, data generation and data analysis; E.D., K.P.M., B.E.P.H., M.B., J.A.M. and N.T.L.

performed data generation and analysis; J.R.P. generated the interactive online browser; M.E. and R.V-T. assisted with CellPhoneDB analyses and critically appraised the manuscript; T.J.K. performed pathological assessments and provided intellectual contribution; N.O.C., J.A.F. and P.N.N. provided intellectual contribution; C.J.W. performed tissue procurement, data generation, interpretation and intellectual contribution; J.R.W-K. performed computational analysis with assistance from J.R.P and R.S.T. and advice from C.P.P., J.M. and S.A.T.; J.R.W-K. also helped with manuscript preparation and C.P.P., J.M. and S.A.T. critically appraised the manuscript; E.M.H., D.J.M. and S.J.W. procured human liver tissue and critically appraised the manuscript. J.P.I., F.T. and J.W.P. provided intellectual contribution and critically appraised the manuscript; N.C.H. conceived the study, designed experiments, interpreted data and prepared the manuscript.

Author Information

The authors declare no competing financial interests.

References

1. Marcellin, P. & Kutala, B. K. Liver diseases: A major, neglected global public health problem requiring urgent actions and large-scale screening. *Liver Int.* (2018). doi:10.1111/liv.13682
2. Hernandez-Gea, V. & Friedman, S. L. Pathogenesis of Liver Fibrosis. *Annu. Rev. Pathol. Mech. Dis.* **6**, 425–456 (2011).
3. Angulo, P. *et al.* Liver Fibrosis, but No Other Histologic Features, Is Associated With Long-term Outcomes of Patients With Nonalcoholic Fatty Liver Disease. *Gastroenterology* **149**, 389-397.e10 (2015).
4. Ramachandran, P. & Henderson, N. C. Antifibrotics in chronic liver disease: tractable targets and translational challenges. *The Lancet Gastroenterology and Hepatology* **1**, 328–340 (2016).
5. Friedman, S. L., Neuschwander-Tetri, B. A., Rinella, M. & Sanyal, A. J. Mechanisms of NAFLD development and therapeutic strategies. *Nature Medicine* **24**, 908–922 (2018).
6. Trautwein, C., Friedman, S. L., Schuppan, D. & Pinzani, M. Hepatic fibrosis: Concept to treatment. *Journal of Hepatology* **62**, S15–S24 (2015).
7. Yukinori Koyama and David A. Brenner. Liver inflammation and fibrosis. *J. Clin. Invest.* **5**, 55–64 (2017).
8. Stubbington, M. J. T., Rozenblatt-Rosen, O., Regev, A. & Teichmann, S. A. Single-cell transcriptomics to explore the immune system in health and disease. *Science* **358**, 58–63 (2017).
9. Giladi, A. & Amit, I. Single-Cell Genomics: A Stepping Stone for Future Immunology Discoveries. *Cell* **172**, 14–21 (2018).
10. Halpern, K. B. *et al.* Single-cell spatial reconstruction reveals global division of labour in the mammalian liver. *Nature* **542**, 352–356 (2017).
11. MacParland, S. A. *et al.* Single cell RNA sequencing of human liver reveals distinct intrahepatic macrophage populations. *Nat. Commun.* **9**, 4383 (2018).
12. Searle, B. C., Gittelman, R. M., Manor, O. & Akey, J. M. Detecting sources of transcriptional heterogeneity in large-scale RNA-seq data sets. *Genetics* **204**, 1391–1396 (2016).
13. Wynn, T. A., Chawla, A. & Pollard, J. W. Macrophage biology in

development, homeostasis and disease. *Nature* **496**, 445–455 (2013).
14. Duffield, J. S. *et al.* Selective depletion of macrophages reveals distinct, opposing roles during liver injury and repair. *J. Clin. Invest.* **115**, 56–65 (2005).
15. Ramachandran, P. *et al.* Differential Ly-6C expression identifies the recruited macrophage phenotype, which orchestrates the regression of murine liver fibrosis. *Proc. Natl. Acad. Sci.* **109**, E3186–E3195 (2012).
16. Zimmermann, H. W. *et al.* Functional Contribution of Elevated Circulating and Hepatic Non-Classical CD14+CD16+ Monocytes to Inflammation and Human Liver Fibrosis. *PLoS One* **5**, e11049 (2010).
17. Beattie, L. *et al.* Bone marrow-derived and resident liver macrophages display unique transcriptomic signatures but similar biological functions. *J. Hepatol.* **65**, 758–768 (2016).
18. Minutti, C. M. *et al.* Local amplifiers of IL-4Rα–mediated macrophage activation promote repair in lung and liver. *Science (80-.).* **356**, 1076–1080 (2017).
19. Baek, J.-H. *et al.* IL-34 mediates acute kidney injury and worsens subsequent chronic kidney disease. *J. Clin. Invest.* **125**, 3198–3214 (2015).
20. Pradere, J.-P. *et al.* Hepatic macrophages but not dendritic cells contribute to liver fibrosis by promoting the survival of activated hepatic stellate cells in mice. *Hepatology* **58**, 1461–1473 (2013).
21. Petrasek, J. *et al.* IL-1 receptor antagonist ameliorates inflammasome-dependent alcoholic steatohepatitis in mice. *J. Clin. Invest.* **122**, 3476–3489 (2012).
22. Syn, W. K. *et al.* Osteopontin is induced by hedgehog pathway activation and promotes fibrosis progression in nonalcoholic steatohepatitis. *Hepatology* **53**, 106–115 (2011).
23. Henderson, N. C. *et al.* Galectin-3 regulates myofibroblast activation and hepatic fibrosis. *Proc. Natl. Acad. Sci.* **103**, 5060–5065 (2006).
24. Seki, E. *et al.* CCR2 promotes hepatic fibrosis in mice. *Hepatology* **50**, 185–197 (2009).
25. Wilhelm, A. *et al.* Interaction of TWEAK with Fn14 leads to the progression of fibrotic liver disease by directly modulating hepatic stellate cell proliferation. *J.*

1181 *Pathol.* **239**, 109–121 (2016).
1182 26. Scott, C. L. & Guilliams, M. The role of Kupffer cells in hepatic iron and lipid
1183 metabolism. *J. Hepatol.* (2018). doi:10.1016/j.jhep.2018.02.013
1184 27. Guilliams, M. *et al.* Dendritic cells, monocytes and macrophages: A unified
1185 nomenclature based on ontogeny. *Nature Reviews Immunology* **14**, 571–578
1186 (2014).
1187 28. Scott, C. L. *et al.* Bone marrow-derived monocytes give rise to self-renewing
1188 and fully differentiated Kupffer cells. *Nat. Commun.* **7**, 10321 (2016).
1189 29. Gomez Perdiguero, E. *et al.* Tissue-resident macrophages originate from yolk-
1190 sac-derived erythro-myeloid progenitors. *Nature* **518**, 547–551 (2015).
1191 30. Hoeffel, G. *et al.* C-Myb^{+} Erythro-Myeloid Progenitor-Derived Fetal
1192 Monocytes Give Rise to Adult Tissue-Resident Macrophages. *Immunity* **42**,
1193 665–678 (2015).
1194 31. Yona, S. *et al.* Fate Mapping Reveals Origins and Dynamics of Monocytes and
1195 Tissue Macrophages under Homeostasis. *Immunity* **38**, 79–91 (2013).
1196 32. Mass, E. *et al.* Specification of tissue-resident macrophages during
1197 organogenesis. *Science* **353**, aaf4238–aaf4238 (2016).
1198 33. Karlmark, K. R. *et al.* Hepatic recruitment of the inflammatory Gr1 +
1199 monocyte subset upon liver injury promotes hepatic fibrosis. *Hepatology* **50**,
1200 261–274 (2009).
1201 34. La Manno, G. *et al.* RNA velocity of single cells. *Nature* 1 (2018).
1202 doi:10.1038/s41586-018-0414-6
1203 35. Klein, A. M. Technique to measure the expression dynamics of each gene in a
1204 single cell. *Nature* **560**, 434–435 (2018).
1205 36. Friedman, S. L. & Arthur, M. J. P. Activation of cultured rat hepatic lipocytes
1206 by Kupffer cell conditioned medium. Direct enhancement of matrix synthesis
1207 and stimulation of cell proliferation via induction of platelet-derived growth
1208 factor receptors. *J. Clin. Invest.* **84**, 1780–1785 (1989).
1209 37. Yang, L. *et al.* Vascular Endothelial Growth Factor Promotes Fibrosis
1210 Resolution and Repair in Mice. *Gastroenterology* **146**, 1339-1350.e1 (2014).
1211 38. Zimmermann, H. W. *et al.* Interleukin-8 is activated in patients with chronic
1212 liver diseases and associated with hepatic macrophage accumulation in human

liver fibrosis. *PLoS One* **6**, e21381 (2011).

39. Butler, A., Hoffman, P., Smibert, P., Papalexi, E. & Satija, R. Integrating single-cell transcriptomic data across different conditions, technologies, and species. *Nat. Biotechnol.* **36**, 411–420 (2018).

40. Scott, C. L. *et al.* The Transcription Factor ZEB2 Is Required to Maintain the Tissue-Specific Identities of Macrophages. *Immunity* **49**, 312-325.e5 (2018).

41. Haldar, M. *et al.* Heme-mediated SPI-C induction promotes monocyte differentiation into iron-recycling macrophages. *Cell* **156**, 1223–1234 (2014).

42. Bradley, E. W., Ruan, M. M. & Oursler, M. J. Novel pro-survival functions of the Kruppel-like transcription factor Egr2 in promotion of macrophage colony-stimulating factor-mediated osteoclast survival downstream of the MEK/ERK pathway. *J. Biol. Chem.* **283**, 8055–64 (2008).

43. Fang, F. *et al.* The Early Growth Response Gene Egr2 (Alias Krox20) Is a Novel Transcriptional Target of Transforming Growth Factor-β that Is Up-Regulated in Systemic Sclerosis and Mediates Profibrotic Responses. *Am. J. Pathol.* **178**, 2077–2090 (2011).

44. Zhang, Q. *et al.* Notch signal suppresses toll-like receptor-triggered inflammatory responses in macrophages by inhibiting extracellular signal-regulated kinase 1/2-mediated nuclear factor κB activation. *J. Biol. Chem.* **287**, 6208–6217 (2012).

45. Ni, M. *et al.* Novel Insights on Notch signaling pathways in liver fibrosis. *Eur. J. Pharmacol.* **826**, 66–74 (2018).

46. Schelker, M. *et al.* Estimation of immune cell content in tumour tissue using single-cell RNA-seq data. *Nat. Commun.* **8**, 2032 (2017).

47. Ahrens, M. *et al.* DNA Methylation Analysis in Nonalcoholic Fatty Liver Disease Suggests Distinct Disease-Specific and Remodeling Signatures after Bariatric Surgery. *Cell Metab.* **18**, 296–302 (2013).

48. Ding, B. Sen *et al.* Divergent angiocrine signals from vascular niche balance liver regeneration and fibrosis. *Nature* **505**, 97–102 (2014).

49. Xie, G. *et al.* Role of differentiation of liver sinusoidal endothelial cells in progression and regression of hepatic fibrosis in rats. *Gastroenterology* **142**, 918-927 e6 (2012).

50. Weinl, C. *et al.* Elk3 Deficiency Causes Transient Impairment in Post-Natal Retinal Vascular Development and Formation of Tortuous Arteries in Adult Murine Retinae. *PLoS One* **9**, e107048 (2014).
51. Borkham-Kamphorst, E. & Weiskirchen, R. The PDGF system and its antagonists in liver fibrosis. *Cytokine and Growth Factor Reviews* **28**, 53–61 (2016).
52. Liu, S. B. *et al.* Lysyl oxidase activity contributes to collagen stabilization during liver fibrosis progression and limits spontaneous fibrosis reversal in mice. *FASEB J.* **30**, 1599–1609 (2016).
53. Ikenaga, N. *et al.* Selective targeting of lysyl oxidase-like 2 (LOXL2) suppresses hepatic fibrosis progression and accelerates its reversal. *Gut* **66**, 1697–1708 (2017).
54. Thiriot, A. *et al.* Differential DARC/ACKR1 expression distinguishes venular from non-venular endothelial cells in murine tissues. *BMC Biol. 2017 151* **15**, 45 (2017).
55. Pruenster, M. *et al.* The Duffy antigen receptor for chemokines transports chemokines and supports their promigratory activity. *Nat. Immunol.* **10**, 101–8 (2009).
56. Shetty, S., Weston, C. J., Adams, D. H. & Lalor, P. F. A Flow Adhesion Assay to Study Leucocyte Recruitment to Human Hepatic Sinusoidal Endothelium Under Conditions of Shear Stress. *J. Vis. Exp.* (2014). doi:10.3791/51330
57. Géraud, C. *et al.* GATA4-dependent organ-specific endothelial differentiation controls liver development and embryonic hematopoiesis. *J. Clin. Invest.* **127**, 1099–1114 (2017).
58. Knolle, P. A. & Wohlleber, D. Immunological functions of liver sinusoidal endothelial cells. *Cell. Mol. Immunol.* **13**, 347–353 (2016).
59. Fatima, A. *et al.* Foxc1 and Foxc2 deletion causes abnormal lymphangiogenesis and correlates with ERK hyperactivation. *J. Clin. Invest.* **126**, 2437–2451 (2016).
60. Harada, K. *et al.* Identification of targets of Prox1 during in vitro vascular differentiation from embryonic stem cells: functional roles of HoxD8 in lymphangiogenesis. *J. Cell Sci.* **122**, 3923–3930 (2009).

61. Rocha, A. S. *et al.* The Angiocrine Factor Rspondin3 Is a Key Determinant of Liver Zonation. *Cell Rep.* **13**, 1757–1764 (2015).
62. Corada, M. *et al.* Sox17 is indispensable for acquisition and maintenance of arterial identity. *Nat. Commun.* **4**, 2609 (2013).
63. Cuervo, H. *et al.* Endothelial notch signaling is essential to prevent hepatic vascular malformations in mice. *Hepatology* **64**, 1302–1316 (2016).
64. Bahrami, A. J. *et al.* Regulator of G-Protein Signaling-5 Is a Marker of Hepatic Stellate Cells and Expression Mediates Response to Liver Injury. *PLoS One* **9**, e108505 (2014).
65. Vallecillo-García, P. *et al.* Odd skipped-related 1 identifies a population of embryonic fibro-adipogenic progenitors regulating myogenesis during limb development. *Nat. Commun.* **8**, 1218 (2017).
66. Henderson, N. C. *et al.* Targeting of αv integrin identifies a core molecular pathway that regulates fibrosis in several organs. *Nat. Med.* **19**, 1617–1624 (2013).
67. De Minicis, S. *et al.* Gene Expression Profiles During Hepatic Stellate Cell Activation in Culture and In Vivo. *Gastroenterology* **132**, 1937–1946 (2007).
68. Hinz, B. *et al.* Recent Developments in Myofibroblast Biology. *Am. J. Pathol.* **180**, 1340–1355 (2012).
69. Vento-Tormo, R. *et al.* Single-cell reconstruction of the early maternal–fetal interface in humans. *Nat. 2018 5637731* **563**, 347 (2018).
70. Liang, D. *et al.* Inhibition of EGFR attenuates fibrosis and stellate cell activation in diet-induced model of nonalcoholic fatty liver disease. *Biochim. Biophys. Acta - Mol. Basis Dis.* **1864**, 133–142 (2018).
71. Minutti, C. M. *et al.* A Macrophage-Pericyte Axis Directs Tissue Restoration via Amphiregulin-Induced Transforming Growth Factor Beta Activation. *Immunity* **50**, 645-654.e6 (2019).
72. Mouchemore, K. A. & Pixley, F. J. CSF-1 signaling in macrophages: pleiotrophy through phosphotyrosine-based signaling pathways. *Crit. Rev. Clin. Lab. Sci.* **49**, 49–61 (2012).
73. Ensan, S. *et al.* Self-renewing resident arterial macrophages arise from embryonic CX3CR1 + precursors and circulating monocytes immediately after

birth. *Nat. Immunol.* **17**, 159–168 (2016).
74. Thabut, D. & Shah, V. Intrahepatic angiogenesis and sinusoidal remodeling in chronic liver disease: New targets for the treatment of portal hypertension? *J. Hepatol.* **53**, 976–980 (2010).
75. Krishnasamy, K. *et al.* Blood vessel control of macrophage maturation promotes arteriogenesis in ischemia. *Nat. Commun.* **8**, 952 (2017).
76. Brenner, D. A. Of mice and men and NASH. *Hepatology* (2018). doi:10.1002/hep.30186
77. Broutier, L. *et al.* Human primary liver cancer–derived organoid cultures for disease modeling and drug screening. *Nat. Med.* **23**, 1424–1435 (2017).

References (Methods)

78. Bain, C. C. *et al.* Long-lived self-renewing bone marrow-derived macrophages displace embryo-derived cells to inhabit adult serous cavities. *Nat. Commun.* **7**, ncomms11852 (2016).
79. Heinrich, M. C. *et al.* Crenolanib Inhibits the Drug-Resistant PDGFRA D842V Mutation Associated with Imatinib-Resistant Gastrointestinal Stromal Tumors. *Clin. Cancer Res.* **18**, 4375–4384 (2012).
80. Mederacke, I., Dapito, D. H., Affò, S., Uchinami, H. & Schwabe, R. F. High-yield and high-purity isolation of hepatic stellate cells from normal and fibrotic mouse livers. *Nat. Protoc.* **10**, 305–315 (2015).
81. Patten, D. A. *et al.* SCARF-1 promotes adhesion of CD4+ T cells to human hepatic sinusoidal endothelium under conditions of shear stress. *Sci. Rep.* **7**, 17600 (2017).
82. Schindelin, J. *et al.* Fiji: an open-source platform for biological-image analysis. *Nat. Methods* **9**, 676–682 (2012).
83. Bankhead, P. *et al.* QuPath: Open source software for digital pathology image analysis. *Sci. Rep.* **7**, 16878 (2017).
84. Arganda-Carreras, I. *et al.* Trainable Weka Segmentation: A machine learning tool for microscopy pixel classification. *Bioinformatics* **33**, 2424–2426 (2017).
85. Kleiner, D. E. *et al.* Design and validation of a histological scoring system for nonalcoholic fatty liver disease. *Hepatology* **41**, 1313–1321 (2005).

86. Deroulers, C. *et al.* Analyzing huge pathology images with open source software. *Diagn. Pathol.* **8**, 92 (2013).
87. Kendall, T. J. *et al.* Hepatic elastin content is predictive of adverse outcome in advanced fibrotic liver disease. *Histopathology* **73**, 90–100 (2018).
88. Satija, R., Farrell, J. A., Gennert, D., Schier, A. F. & Regev, A. Spatial reconstruction of single-cell gene expression data. *Nat. Biotechnol.* **33**, 495–502 (2015).
89. Haber, A. L. *et al.* A single-cell survey of the small intestinal epithelium. *Nature* (2017). doi:10.1038/nature24489
90. Li, W. V. & Li, J. J. An accurate and robust imputation method scImpute for single-cell RNA-seq data. *Nat. Commun.* **9**, 997 (2018).
91. Camp, J. G. *et al.* Multilineage communication regulates human liver bud development from pluripotency. *Nature* **546**, 533–538 (2017).
92. Trapnell, C. *et al.* The dynamics and regulators of cell fate decisions are revealed by pseudotemporal ordering of single cells. *Nat. Biotechnol.* **32**, 381–386 (2014).
93. McCarthy, D. J., Campbell, K. R., Lun, A. T. L. & Wills, Q. F. Scater: Pre-processing, quality control, normalization and visualization of single-cell RNA-seq data in R. *Bioinformatics* **33**, 1179–1186 (2017).
94. Zhang, H. M. *et al.* AnimalTFDB 2.0: A resource for expression, prediction and functional study of animal transcription factors. *Nucleic Acids Res.* **43**, D76–D81 (2015).
95. Aibar, S. *et al.* SCENIC: Single-cell regulatory network inference and clustering. *Nat. Methods* **14**, 1083–1086 (2017).
96. Newman, A. M. *et al.* Robust enumeration of cell subsets from tissue expression profiles. *Nat. Methods* (2015). doi:10.1038/nmeth.3337

Figure 1: Single cell atlas of human liver non-parenchymal cells.

a, Overview: extraction of non-parenchymal cells (NPC) from healthy or cirrhotic human liver, followed by fluorescence-activated cell sorting (FACS) into leucocyte ($CD45^+$) and other NPC fractions ($CD45^-$) for droplet-based 3' single-cell RNA-seq. **b**, t-SNE visualisation: clustering (colour) 66,135 non-parenchymal cells (points; n=5 healthy and n=5 cirrhotic human livers). **c**, t-SNE visualisation: injury condition (colour; healthy *versus* cirrhotic). **d**, t-SNE visualisation: cell lineage (colour) inferred from expression of known marker gene signatures. Endo, endothelial cell; ILC, innate lymphoid cell; Mast, mast cell; Mes, mesenchymal cell; MP, mononuclear phagocyte; pDC, plasmacytoid dendritic cell. **e**, Scaled heatmap (red, high; blue, low): cluster marker genes (top, colour coded and numbered by cluster and colour coded by condition) and exemplar genes and lineage annotation labelled (right). Cells columns, genes rows.

Figure 1

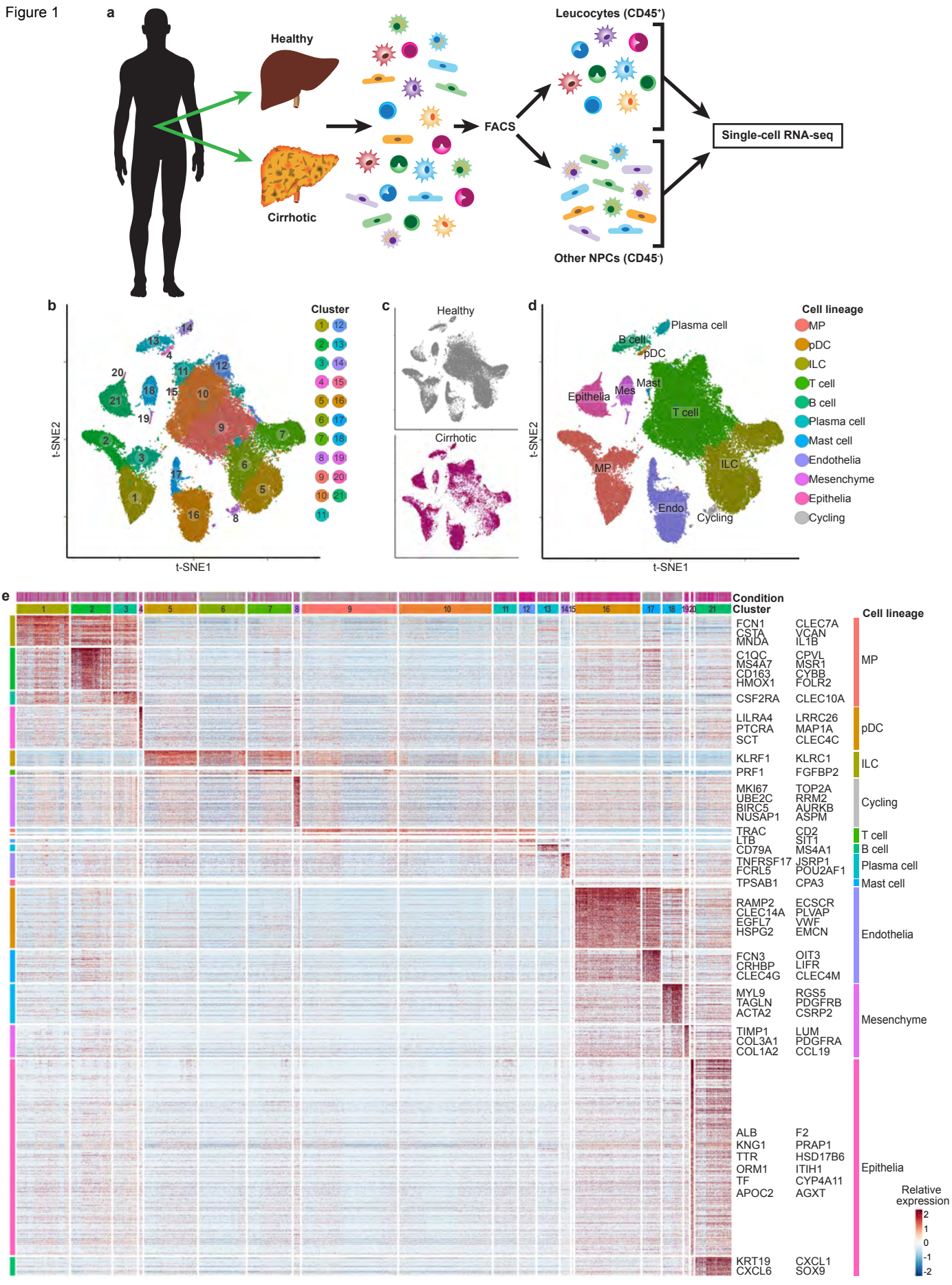
a
Healthy
Cirrhotic
FACS
Leucocytes (CD45+)
Other NPCs (CD45-)
Single-cell RNA-seq
b
t-SNE2
t-SNE1
Cluster
c
Healthy
Cirrhotic
d
Plasma cell
B cell
pDC
Mast
Epithelia
Mes
T cell
MP
ILC
Endo
Cycling
Cell lineage
MP
pDC
ILC
T cell
B cell
Plasma cell
Mast cell
Endothelia
Mesenchyme
Epithelia
Cycling
e
Condition
Cluster
FCN1 CLEC7A
CSTA VCAN
MNDA IL1B
C1QC CPVL
MS4A7 MSR1
CD163 CYBB
HMOX1 FOLR2
CSF2RA CLEC10A
LILRA4 LRRC26
PTCRA MAP1A
SCT CLEC4C
KLRF1 KLRC1
PRF1 FGFBP2
MKI67 TOP2A
UBE2C RRM2
BIRC5 AURKB
NUSAP1 ASPM
TRAC CD2
LTB SIT1
CD79A MS4A1
TNFRSF17 JSRP1
FCRL5 POU2AF1
TPSAB1 CPA3
RAMP2 ECSCR
CLEC14A PLVAP
EGFL7 VWF
HSPG2 EMCN
FCN3 OIT3
CRHBP LIFR
CLEC4G CLEC4M
MYL9 RGS5
TAGLN PDGFRB
ACTA2 CSRP2
TIMP1 LUM
COL3A1 PDGFRA
COL1A2 CCL19
ALB F2
KNG1 PRAP1
TTR HSD17B6
ORM1 ITIH1
TF CYP4A11
APOC2 AGXT
KRT19 CXCL1
CXCL6 SOX9
Cell lineage
MP
pDC
ILC
Cycling
T cell
B cell
Plasma cell
Mast cell
Endothelia
Mesenchyme
Epithelia
Relative expression
2
1
0
-1
-2

Figure 2: Identifying scar-associated macrophage subpopulations.

a, t-SNE visualisation: clustering 10,737 mononuclear phagocytes (MP) into 10 clusters (colour and number). Annotation of clusters (identity). TMo, tissue monocyte; SAM, scar-associated macrophage; KC, Kupffer cell; cDC, conventional dendritic cell. **b**, t-SNE visualisation: annotating MP cells by injury condition (colour). **c**, Fractions of MP subpopulations in healthy (n=5) *versus* cirrhotic (n=5) livers, Wald test. **d**, Scaled heatmap (red, high; blue, low): MP cluster marker genes (top, colour coded by cluster and condition), exemplar genes labelled (right). Cells columns, genes rows. **e**, Violin plots: scar-associated macrophage and tissue monocyte cluster markers. **f**, Representative flow cytometry plots: quantifying $TREM2^{+}CD9^{+}$ MP fraction by flow cytometry in healthy (n=2) *versus* cirrhotic (n=3) liver, Wald. **g**, Representative immunofluorescence micrograph, cirrhotic liver: TREM2 (red), CD9 (white), collagen 1 (green), DAPI (blue). Scale bar, 50μm. **h**, Automated cell counting: TREM2 staining, healthy (n=10) *versus* cirrhotic (n=9) liver, Mann-Whitney. **i**, Automated cell counting: CD9 staining, healthy (n=12) *versus* cirrhotic (n=10) liver, Mann-Whitney. **j**, Topographically assessing scar-associated macrophages: exemplar tissue segmentation (left), stained section morphologically segmented into fibrotic septae (orange) and parenchymal nodules (purple)). $TREM2^{+}$, $CD9^{+}$, $TIMD4^{+}$ and $MARCO^{+}$ automated cell counts (right) in parenchymal nodules *versus* fibrotic septae, Wilcoxon. Error bars, s.e.m.; * p-value<0.05; ** p-value < 0.01; *** p-value < 0.001.

Figure 2

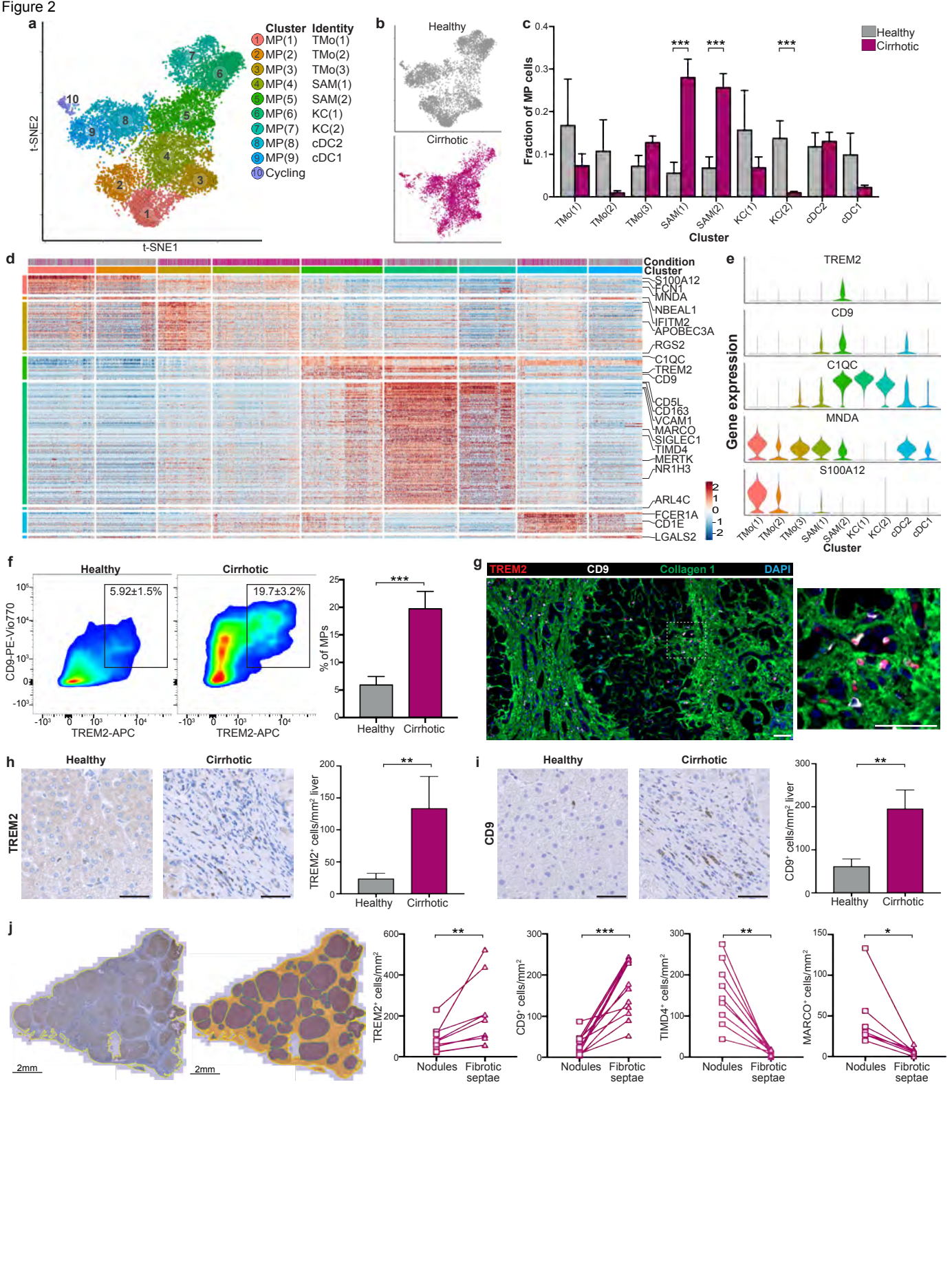
a
t-SNE2
t-SNE1
Cluster Identity
1 MP(1) TMo(1)
2 MP(2) TMo(2)
3 MP(3) TMo(3)
4 MP(4) SAM(1)
5 MP(5) SAM(2)
6 MP(6) KC(1)
7 MP(7) KC(2)
8 MP(8) cDC2
9 MP(9) cDC1
10 Cycling
b
Healthy
Cirrhotic
c
Fraction of MP cells
Healthy
Cirrhotic
***
TMo(1) TMo(2) TMo(3) SAM(1) SAM(2) KC(1) KC(2) cDC2 cDC1
Cluster
d
Condition
Cluster
S100A12
FCN1
MNDA
NBEAL1
IFITM2
APOBEC3A
RGS2
C1QC
TREM2
CD9
CD5L
CD163
VCAM1
MARCO
SIGLEC1
TIMD4
MERTK
NR1H3
ARL4C
FCER1A
CD1E
LGALS2
e
Gene expression
TREM2
CD9
C1QC
MNDA
S100A12
TMo(1) TMo(2) TMo(3) SAM(1) SAM(2) KC(1) KC(2) cDC2 cDC1
Cluster
f
Healthy
Cirrhotic
5.92±1.5%
19.7±3.2%
CD9-PE-Vio770
TREM2-APC
% of MPs
***
Healthy Cirrhotic
g
TREM2
CD9
Collagen 1
DAPI
h
Healthy
Cirrhotic
TREM2
TREM2⁺ cells/mm² liver
**
Healthy Cirrhotic
i
Healthy
Cirrhotic
CD9
CD9⁺ cells/mm² liver
**
Healthy Cirrhotic
j
2mm
2mm
TREM2⁺ cells/mm²
**
CD9⁺ cells/mm²
***
TIMD4⁺ cells/mm²
**
MARCO⁺ cells/mm²
*
Nodules Fibrotic septae

Figure 3: Fibrogenic phenotype of scar-associated macrophages.

a, Self-Organising Map (SOM; 60x60 grid): smoothed scaled metagene expression of mononuclear phagocyte (MP) lineage. 20,952 genes, 3,600 metagenes, 44 signatures. A-F label metagene signatures overexpressed in one or more MP subpopulations. **b**, Radar plots (left): metagene signatures A-C showing distribution of signature expression across MP subpopulations, exemplar genes (middle) and Gene Ontology (GO) enrichment (right). **c**, Diffusion map visualisation, blood monocytes and liver-resident MP lineages (23,075 cells), annotating *monocle* pseudotemporal dynamics (purple to yellow). RNA velocity field (red arrows) visualised using Gaussian smoothing on regular grid. Below: Annotation of MP subpopulation, injury condition. **d**, UMAP visualisation, blood monocytes and liver-resident MP lineages, annotating *monocle* pseudotemporal dynamics (purple to yellow). RNA velocity field (red arrows) visualised using Gaussian smoothing on regular grid. Below: Annotation of MP subpopulation, injury condition. **e**, Unspliced-spliced phase portraits (top row), cells coloured as in **d**, for monocyte (*MNDA*), SAM (*CD9*) and KC marker genes (*TIMD4*). Cells plotted above or below the steady-state (black dashed line) indicate increasing or decreasing expression of gene, respectively. Spliced expression profile for genes (middle row; red high, blue low). Unspliced residuals (bottom row), positive (red) indicating expected upregulation, negative (blue) indicating expected downregulation for genes. *MNDA* displays negative velocity in SAM, *CD9* displays positive velocity in monocytes and SAM, *TIMD4* velocity is restricted to KC. **f**, UMAP visualisation, transition probabilities per SAM subpopulation, indicating for each cell the likelihood of transition into either SAM(1) or SAM(2), calculated using RNA velocity (yellow high; purple low; grey below threshold of $2x10^{-4}$). **g**, Scaled heatmap (red, high; blue low): cubic smoothing spline curves fitted to genes differentially expressed across blood monocyte-to-SAM (right arrow) and blood monocyte-to-cDC (left arrow) pseudotemporal trajectories, grouped by hierarchical clustering (k=3). Gene co-expression modules (colour) labelled right. **h**, Cubic smoothing spline curve fitted to averaged expression of all genes in module 1, along monocyte-SAM pseudotemporal trajectory, selected GO enrichment (right) and curves fit to exemplar genes (below).

Figure 3

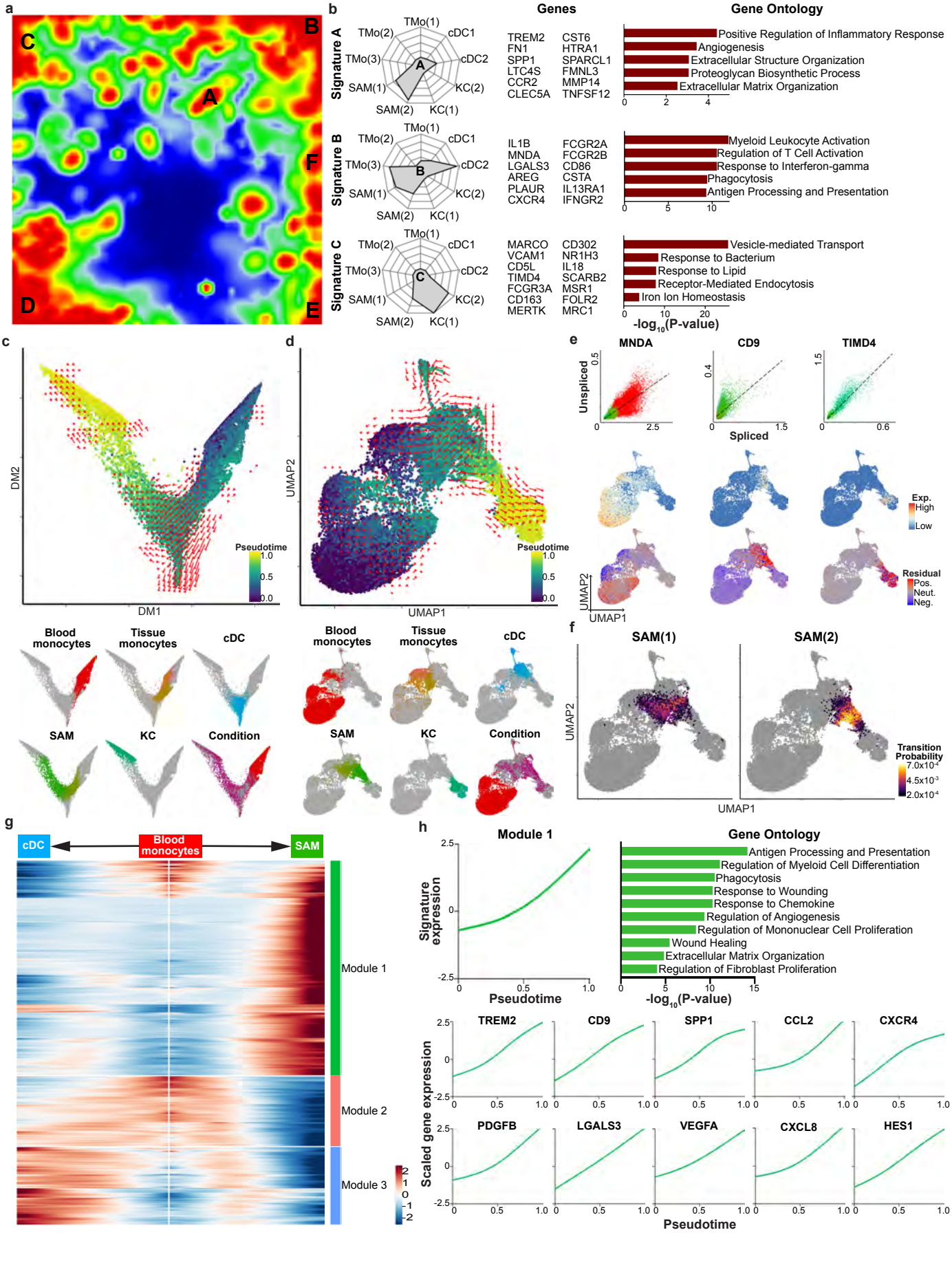
a
b
Genes
Gene Ontology
Signature A
TMo(1)
TMo(2)
TMo(3)
SAM(1)
SAM(2)
cDC1
cDC2
KC(2)
KC(1)
TREM2 CST6
FN1 HTRA1
SPP1 SPARCL1
LTC4S FMNL3
CCR2 MMP14
CLEC5A TNFSF12
Positive Regulation of Inflammatory Response
Angiogenesis
Extracellular Structure Organization
Proteoglycan Biosynthetic Process
Extracellular Matrix Organization
Signature B
IL1B FCGR2A
MNDA FCGR2B
LGALS3 CD86
AREG CSTA
PLAUR IL13RA1
CXCR4 IFNGR2
Myeloid Leukocyte Activation
Regulation of T Cell Activation
Response to Interferon-gamma
Phagocytosis
Antigen Processing and Presentation
Signature C
MARCO CD302
VCAM1 NR1H3
CD5L IL18
TIMD4 SCARB2
FCGR3A MSR1
CD163 FOLR2
MERTK MRC1
Vesicle-mediated Transport
Response to Bacterium
Response to Lipid
Receptor-Mediated Endocytosis
Iron Ion Homeostasis
-log10(P-value)
c
DM2
DM1
Pseudotime
d
UMAP2
UMAP1
e
MNDA
CD9
TIMD4
Unspliced
Spliced
Exp.
High
Low
Residual
Pos.
Neut.
Neg.
Blood monocytes
Tissue monocytes
cDC
SAM
KC
Condition
f
SAM(1)
SAM(2)
Transition Probability
g
cDC
Blood monocytes
SAM
Module 1
Module 2
Module 3
h
Module 1
Signature expression
Pseudotime
Gene Ontology
Antigen Processing and Presentation
Regulation of Myeloid Cell Differentiation
Phagocytosis
Response to Wounding
Response to Chemokine
Regulation of Angiogenesis
Regulation of Mononuclear Cell Proliferation
Wound Healing
Extracellular Matrix Organization
Regulation of Fibroblast Proliferation
TREM2
CD9
SPP1
CCL2
CXCR4
PDGFB
LGALS3
VEGFA
CXCL8
HES1
Scaled gene expression

Figure 4: Identifying scar-associated endothelial subpopulations.

a, t-SNE visualisation: clustering 8,020 endothelial cells, annotating injury condition. **b**, Fractions of endothelial subpopulations in healthy (n=4) *versus* cirrhotic (n=3) livers, Wald. **c**, Scaled heatmap (red, high; blue, low): endothelial cluster marker genes (colour coded top by cluster and condition), exemplar genes labelled right. Cells columns, genes rows. **d**, Representative immunofluorescence micrograph, healthy *versus* cirrhotic liver: CD34 (red), CLEC4M (white), PLVAP (green), DAPI (blue). **e**, Representative immunofluorescence micrographs, healthy *versus* cirrhotic liver: RSPO3, PDPN, AIF1L, VWA1 or ACKR1 (red), CD34 (white), PLVAP (green), DAPI (blue). **f**, Digital morphometric pixel quantification: CLEC4M staining healthy (n=5) *versus* cirrhotic (n=8), PLVAP staining healthy (n=11) *versus* cirrhotic (n=11), ACKR1 staining healthy (n=10) *versus* cirrhotic (n=10), Mann-Whitney. **g**, Scaled heatmap (red, high; blue, low): endothelial cluster marker transcription factor regulons (colour coded top by cluster and condition), exemplar regulons labelled right. Cells in columns, regulons in rows. Scale bars, 50μm. Error bars, s.e.m.; * p-value < 0.05, ** p-value < 0.01, *** p-value < 0.001.

Figure 4

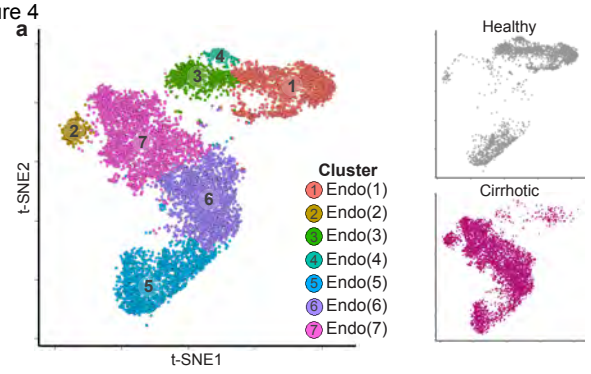
a
Healthy
Cirrhotic
t-SNE2
t-SNE1
Cluster
1 Endo(1)
2 Endo(2)
3 Endo(3)
4 Endo(4)
5 Endo(5)
6 Endo(6)
7 Endo(7)

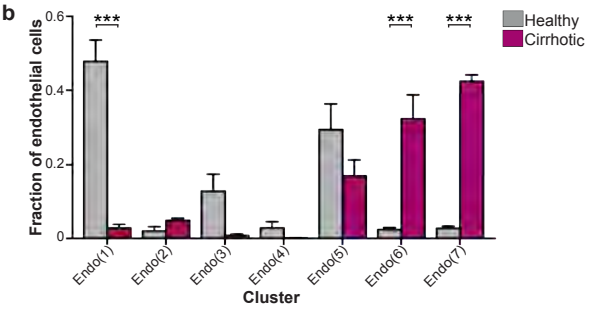
b
Fraction of endothelial cells
0.6
0.4
0.2
0
***
***
***
Healthy
Cirrhotic
Endo(1)
Endo(2)
Endo(3)
Endo(4)
Endo(5)
Endo(6)
Endo(7)
Cluster


c
Condition
Cluster
CLEC4G
CLEC4M
STAB2
MRC1
CD14
LYVE1
CCL21
PROX1
PDPN
CPE
CD320
BMPER
RSPO3
WNT2
LHX6
HTR2B
SOX17
AIF1L
PLVAP
VWA1
ACKR1
2
1
0
-1
-2

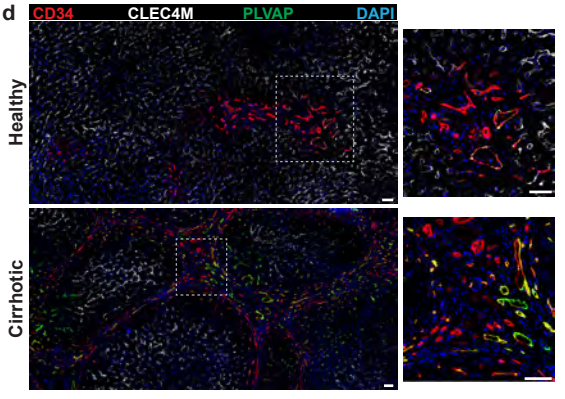
d
CD34
CLEC4M
PLVAP
DAPI
Healthy
Cirrhotic

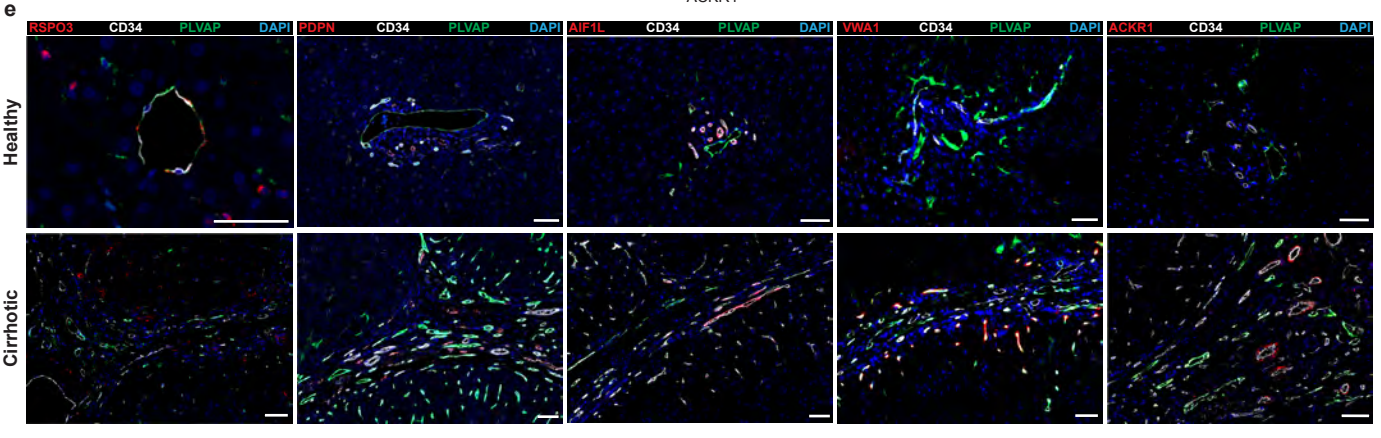
e
RSPO3
PDPN
AIF1L
VWA1
ACKR1
CD34
PLVAP
DAPI
Healthy
Cirrhotic

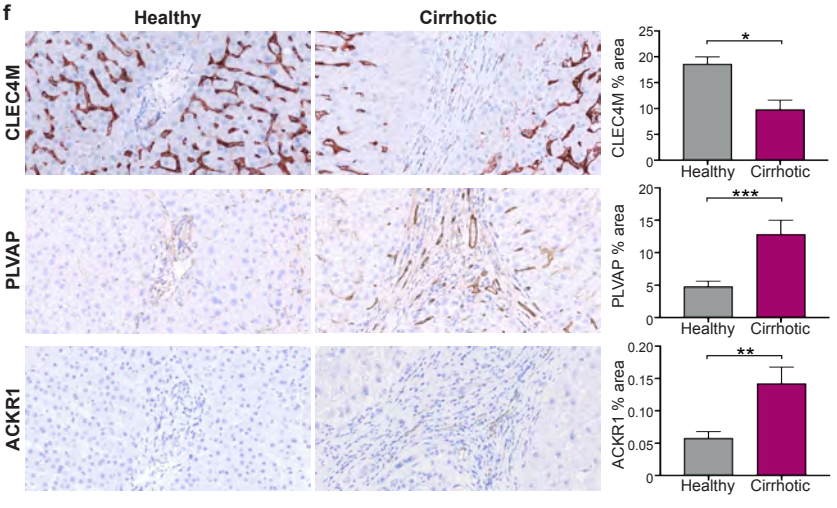
f
Healthy
Cirrhotic
CLEC4M
PLVAP
ACKR1

CLEC4M % area
25
20
15
10
5
0
*
Healthy
Cirrhotic
PLVAP % area
20
15
10
5
0
***
Healthy
Cirrhotic
ACKR1 % area
0.20
0.15
0.10
0.05
0
**
Healthy
Cirrhotic


g
Condition
Cluster
GATA4
NR5A2
STAT2
RARB
IRF1
ATF3
MEF2C
HOXD8
HOXD9
FOXC2
HOXA9
GATA6
PPARA
SOX17
KLF2
FOXP1
ELK3
JDP2
2
1
0
-1
-2

Figure 5: Identifying scar-associated mesenchymal cell populations.

a, t-SNE visualisation: clustering 2,318 mesenchymal cells (Mes) into 4 clusters (colour and number). Annotation of clusters (identity). VSMC, vascular smooth muscle cell; HSC, hepatic stellate cell; SAMes, scar-associated mesenchymal cell. Annotation by injury condition (colour). **b**, Scaled heatmap (red, high; blue, low): Mes cluster marker genes (top, colour coded by cluster and condition), exemplar genes labelled (right). Cells columns, genes rows. **c**, Representative immunofluorescence micrograph, healthy *versus* cirrhotic liver: RGS5 (red), MYH11 (white), PDGFRα (green), DAPI (blue). **d**, Violin plots: fibrillar collagen expression in mesenchymal cell clusters. **e**, Fractions of mesenchymal subpopulations in healthy (n=4) *versus* cirrhotic (n=3) livers, Wald. **f**, Digital morphometric pixel quantification: PDGFRα staining, healthy (n=11) *versus* cirrhotic (n=11) liver (top), Mann-Whitney. Topographically assessing PDGFRα staining, stained cirrhotic sections (n=10) morphologically segmented into fibrotic septae and parenchymal nodules (bottom), Wilcoxon. Scale bars, 50μm. Error bars, s.e.m.; * p-value<0.05; ** p-value < 0.01; *** p-value < 0.001.

Figure 5

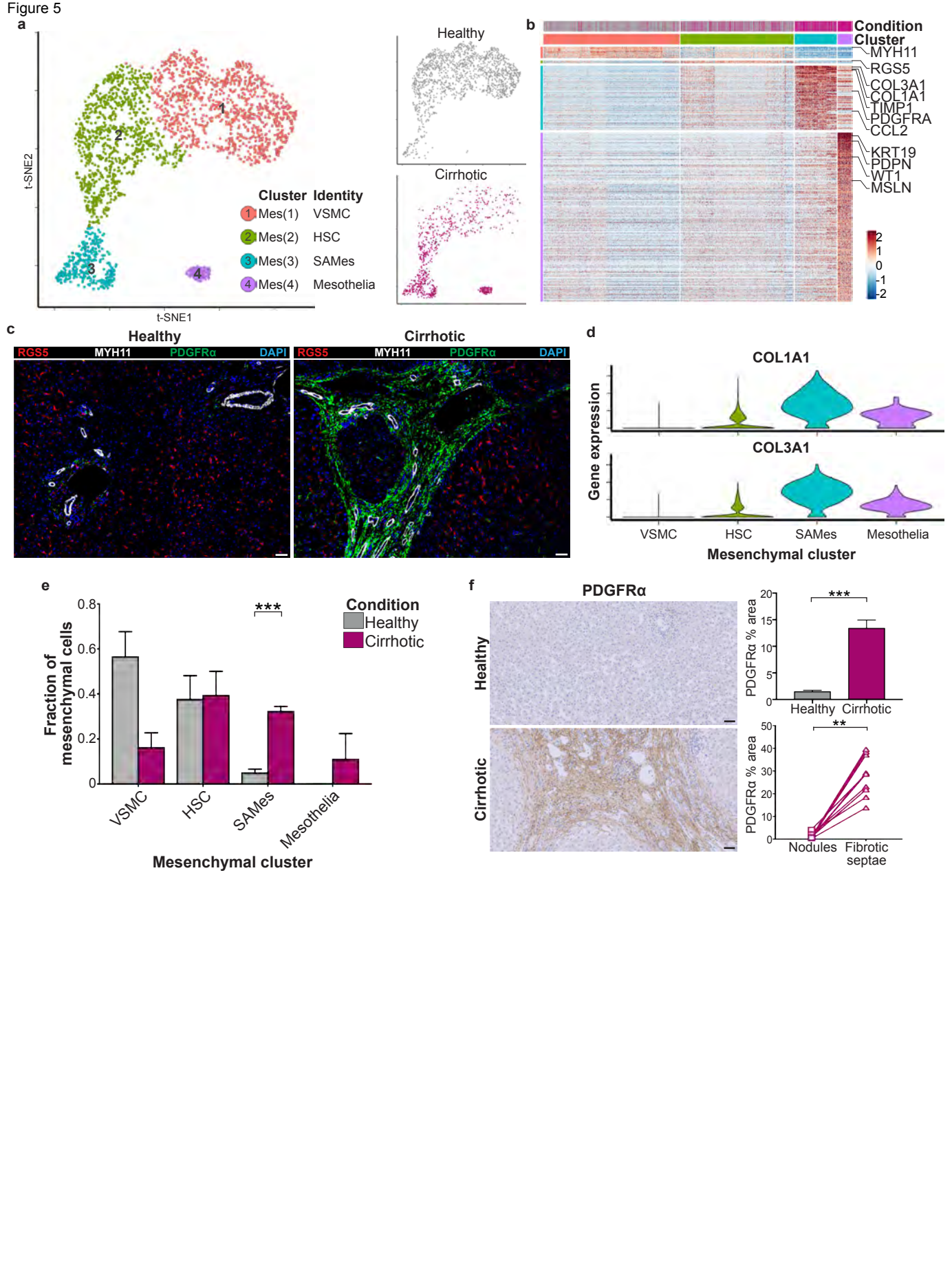
a
t-SNE2
t-SNE1
Cluster Identity
1 Mes(1) VSMC
2 Mes(2) HSC
3 Mes(3) SAMes
4 Mes(4) Mesothelia
Healthy
Cirrhotic
b
Condition
Cluster
MYH11
RGS5
COL3A1
COL1A1
TIMP1
PDGFRA
CCL2
KRT19
PDPN
WT1
MSLN
2
1
0
-1
-2
c
Healthy
Cirrhotic
RGS5
MYH11
PDGFRα
DAPI
d
COL1A1
COL3A1
Gene expression
VSMC
HSC
SAMes
Mesothelia
Mesenchymal cluster
e
Fraction of mesenchymal cells
0.8
0.6
0.4
0.2
0
***
Condition
Healthy
Cirrhotic
VSMC
HSC
SAMes
Mesothelia
Mesenchymal cluster
f
PDGFRα
Healthy
Cirrhotic
PDGFRα % area
20
15
10
5
0
***
Healthy
Cirrhotic
50
40
30
20
10
0
**
Nodules
Fibrotic septae

Figure 6: Multi-lineage interactions in the fibrotic niche.

a to b, Representative immunofluorescence micrographs, fibrotic niche. **a**, TREM2 (red), PLVAP (white), PDGFRα (green), DAPI (blue). **b**, TREM2 (red), ACKR1 (white), PDGFRα (green), DAPI (blue). **c**, Dotplot: ligand-receptor interactions between scar-associated macrophages (SAM) and scar-associated mesenchyme (SAMes). X-axis, ligand (red) and cognate receptor (blue); y-axis, cell populations expressing ligand (red) and receptor (blue); circle size, p-value; colour (red, high; yellow, low), means of average ligand and receptor expression levels in interacting subpopulations. **d to e**, Representative immunofluorescence micrographs, fibrotic niche. **d**, TREM2 (red), PDGFB (white), PDGFRα (green), DAPI (blue), arrows $TREM2^{+}PDGFB^{+}$ cells. **e**, TNFRSF12A (red), TNFSF12 (white), PDGFRα (green), DAPI (blue), arrows $TNFRSF12A^{+}PDGFR\alpha^{+}$ cells. **f to h**, Hepatic stellate cell (HSC) proliferation assay: y-axis, area under curve (AUC) of % change in HSC number over time (hours), one-way ANOVA and Tukey. **f**, Vehicle, PDGF-BB (10ng/ml), Crenolanib (1μM), all n=3. **g**, Control, TNFSF12 (100ng/ml), anti-TNFRSF12A (2μg/ml), isotype control (2μg/ml), all n=3. **h**, Conditioned media from hepatic macrophages; SAM, tissue monocytes (TMo), Kupffer cells (KC), control, all n=2. **i**, Dotplot: ligand-receptor interactions between scar-associated endothelial cells (SAEndo) and SAMes. X-axis, ligand (red) and cognate receptor (blue); y-axis, cell populations expressing ligand (red) and receptor (blue); circle size, p-value; colour (red, high; yellow, low), means of average ligand and receptor expression levels in interacting subpopulations. **j**, Endothelial cell JAG1 flow cytometry: healthy (n=3) or cirrhotic (n=9) liver, representative histogram (top), mean fluorescence intensity (MFI, bottom), Mann-Whitney. **k**, Representative immunofluorescence micrographs, fibrotic niche. NOTCH3 (red), DLL4 (white), PDGFRα (green), DAPI (blue), arrows $NOTCH3^{+}PDGFR\alpha^{+}$ cells. **l to m**, Cirrhotic endothelial cell and HSC co-culture, Notch inhibitor Dibenzazepine (DBZ; 10μM). **l**, Representative immunofluorescence micrographs, Collagen 1 (magenta), PECAM1 (green), DAPI (blue). **m**, Digital pixel analysis; collagen 1 area, n=3 per condition, RM one-way ANOVA and Tukey. **n**, HSC gene knockdown: control (n=7) or *NOTCH3* (n=7) siRNA, qPCR of stated gene, expression relative to mean expression of control siRNA, Mann-Whitney. Scale bars, 50μm. Error bars, s.e.m.; * p-value<0.05; ** p-value < 0.01; *** p-value < 0.001.

Figure 6

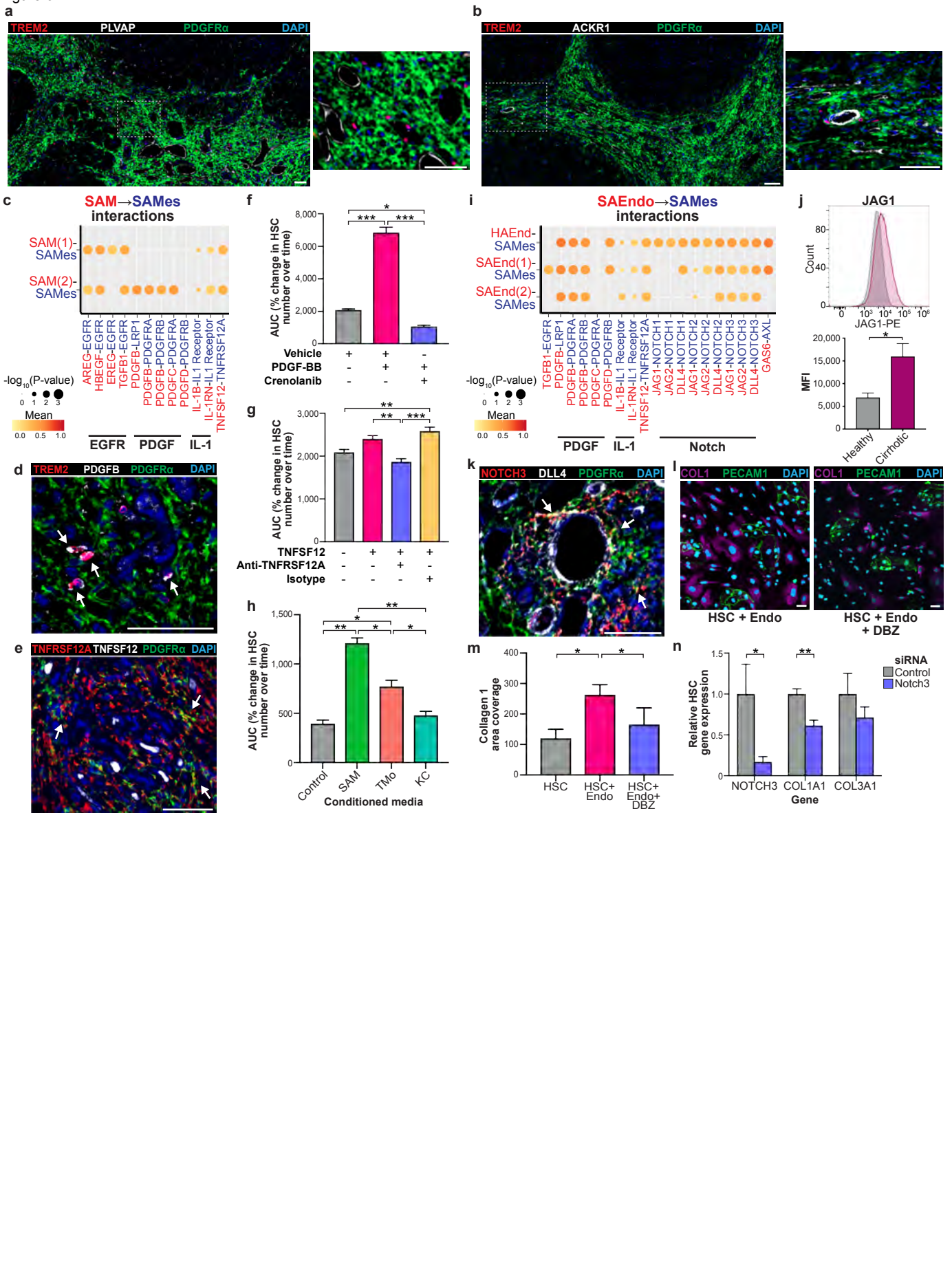
a
TREM2 PLVAP PDGFRα DAPI
b
TREM2 ACKR1 PDGFRα DAPI
c
SAM→SAMes interactions
SAM(1)-SAMes
SAM(2)-SAMes
AREG-EGFR
HBEGF-EGFR
EREG-EGFR
TGFB1-EGFR
PDGFB-LRP1
PDGFB-PDGFRA
PDGFB-PDGFRB
PDGFC-PDGFRA
PDGFD-PDGFRB
IL-1B-IL1 Receptor
IL-1RN-IL1 Receptor
TNFSF12-TNFRSF12A
-log10(P-value)
Mean
EGFR
PDGF
IL-1
d
TREM2 PDGFB PDGFRα DAPI
e
TNFRSF12A TNFSF12 PDGFRα DAPI
f
AUC (% change in HSC number over time)
Vehicle
PDGF-BB
Crenolanib
g
AUC (% change in HSC number over time)
TNFSF12
Anti-TNFRSF12A
Isotype
h
AUC (% change in HSC number over time)
Control
SAM
TMo
KC
Conditioned media
i
SAEndo→SAMes interactions
HAEnd-SAMes
SAEnd(1)-SAMes
SAEnd(2)-SAMes
TGFB1-EGFR
PDGFB-LRP1
PDGFB-PDGFRA
PDGFB-PDGFRB
PDGFC-PDGFRA
PDGFD-PDGFRB
IL-1B-IL1 Receptor
IL-1RN-IL1 Receptor
TNFSF12-TNFRSF12A
JAG1-NOTCH1
JAG2-NOTCH1
DLL4-NOTCH1
JAG1-NOTCH2
JAG2-NOTCH2
DLL4-NOTCH2
JAG1-NOTCH3
JAG2-NOTCH3
DLL4-NOTCH3
GAS6-AXL
-log10(P-value)
Mean
PDGF
IL-1
Notch
j
JAG1
Count
JAG1-PE
MFI
Healthy
Cirrhotic
k
NOTCH3 DLL4 PDGFRα DAPI
l
COL1 PECAM1 DAPI
HSC + Endo
HSC + Endo + DBZ
m
Collagen 1 area coverage
HSC
HSC+ Endo
HSC+ Endo+ DBZ
n
Relative HSC gene expression
siRNA
Control
Notch3
NOTCH3
COL1A1
COL3A1
Gene

Extended Data Figure 1: Strategy for isolation of human liver non-parenchymal cells.

a, Patient demographics and clinical information. **b**, Representative flow cytometry plots: gating strategy for isolating leucocytes ($CD45^+$) and other non-parenchymal cells ($CD45^-$) from healthy and cirrhotic liver. **c**, Representative flow cytometry plots: gating strategy for isolating peripheral blood mononuclear cells (PBMC). **d**, t-SNE visualisation: clustering 103,568 cells (n=5 healthy human livers, n=5 cirrhotic human livers, n=1 healthy PBMC, n=4 cirrhotic PBMC), annotating source (PBMC *versus* liver) and cell lineage inferred from known marker gene signatures. Endo, endothelial cell; ILC, innate lymphoid cell; Mast, mast cell; Mes, mesenchymal cell; MP, mononuclear phagocyte; pDC, plasmacytoid dendritic cell. **e**, Dotplot: annotating PBMC and liver dataset clusters by lineage signatures. Circle size indicates cell fraction expressing signature greater than mean; colour indicates mean signature expression (red, high; blue, low). **f**, Violin plots: number of unique genes (nGene) and number of total Unique Molecular Identifiers (nUMI) expressed in PBMC. **g**, Pie charts: proportion of cell lineage per PBMC sample. **h**, Box and whisker plot: agreement in expression profiles across PBMC samples. Pearson correlation coefficients between average expression profiles for cell in each lineage, across all pairs of samples. Black bar, median value; box edges, 25^{th} and 75^{th} percentiles; whiskers, full range.

Extended Data Figure 1

a

	Healthy liver (n=5)	Cirrhotic liver (n=5)	Blood (n=4)
Age (yrs)	57.4±7.9	56.6±5.8	63.2±3.8
Gender (M:F)	4:1	3:2	3:1
Aetiology of liver disease	N/A	2xNAFLD 2xALD 1xPBC	3xNAFLD 1xHH
Haemoglobin (g/l)	145±14	106±17	131±2.1
White Cell Count (x10⁹/l)	8.2±2.2	5.9±1.7	3.7±1.5
Platelets (x10⁹/l)	300±91	137±56	73±38
Prothrombin Time (s)	11.6±1.1	19.6±3.8	16.0±3.6
Creatinine (μmol/l)	76.4±14.5	96.8±28.6	74.5±9.7
Na⁺ (mmol/l)	141±2.6	131±7.0	139±2.1
Bilirubin (μmol/l)	10±5.2	79.6±83.5	36.3±20.0
ALT (IU/l)	27.8±19.3	77.8±80.7	96.2±121.0
ALP (IU/l)	122±47	140±80	203±153
MELD Score	6.6±0.5	17.3±4.5	11.7±4.3

NAFLD:Non-alcoholic fatty liver disease; ALD:Alcohol-related liver dsease; PBC:Primary biliary cholangitis; HH:Hereditary haemochromatosis; ALT:Alanine transaminase; ALP:Alkaline Phosphatase; MELD:Model for End-Stage Liver Disease

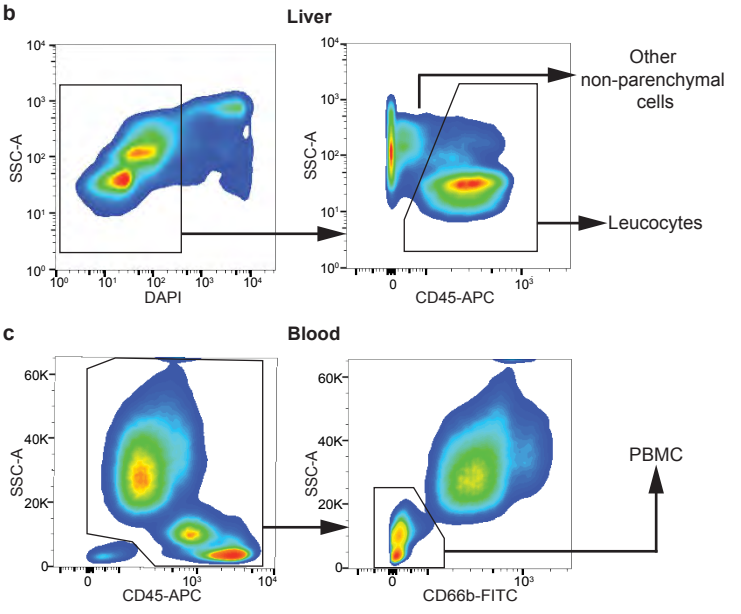

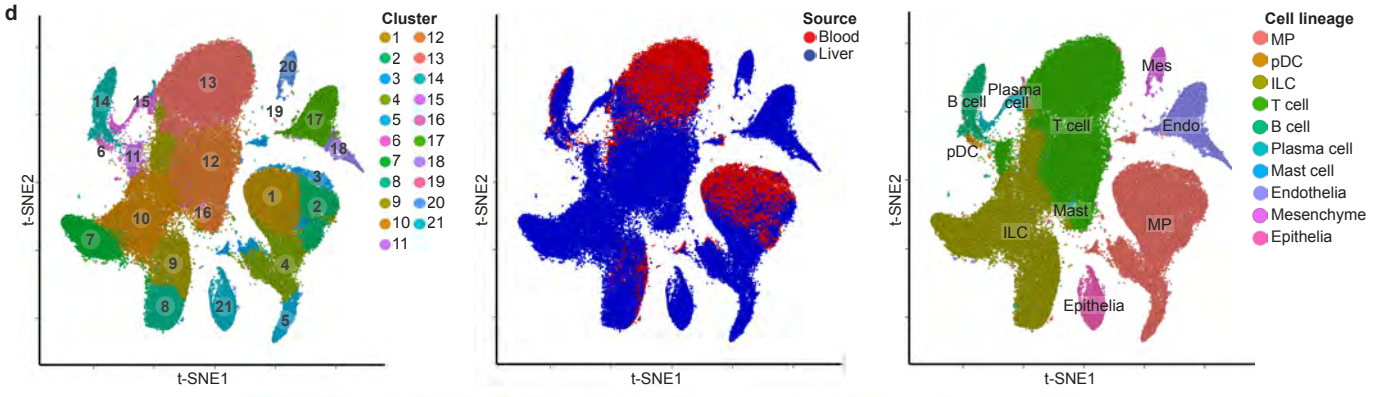

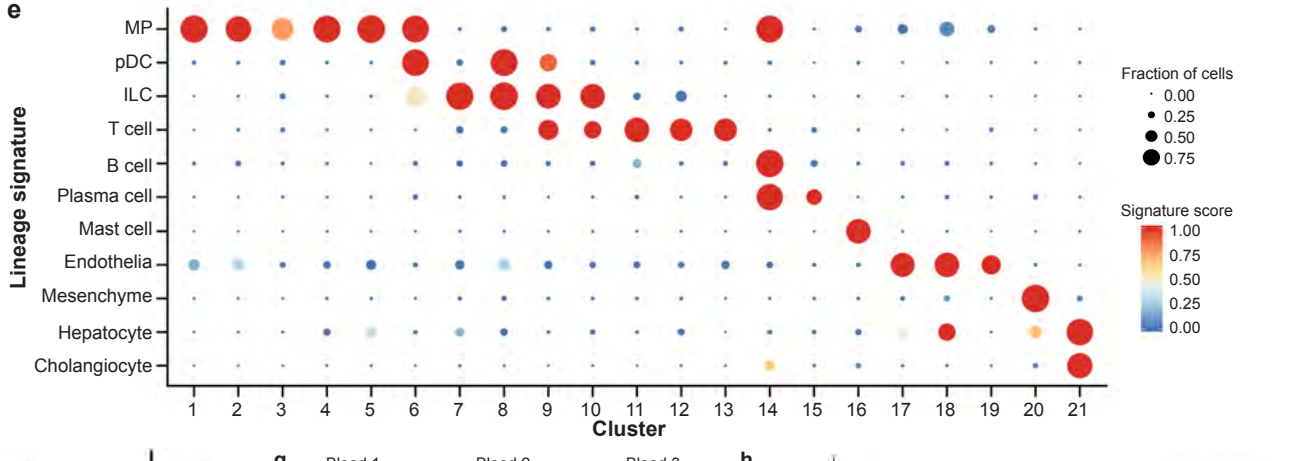

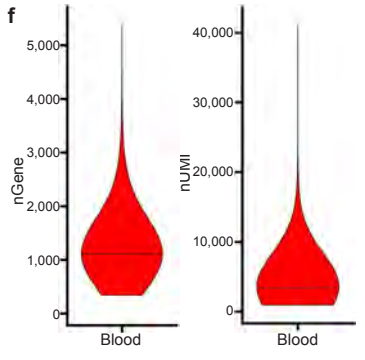

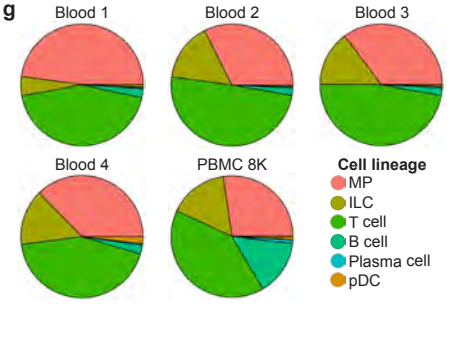

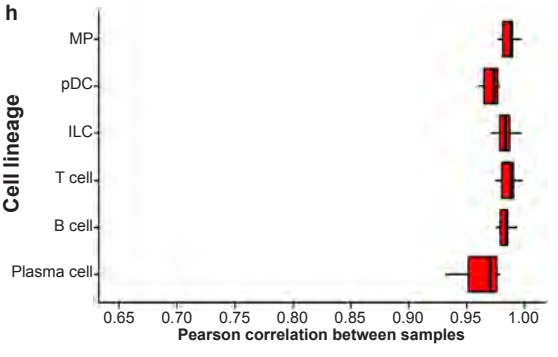

Extended Data Figure 2: Quality control and annotation of human liver-resident cells.

a, t-SNE visualisation: lineage signature expression across liver-resident cell dataset (red, high; blue, low). **b**, Dotplot: annotating liver-resident cell clusters by lineage signature. Circle size indicates cell fraction expressing signature greater than mean; colour indicates mean signature expression (red, high; blue, low). **c**, Violin plot: number of unique genes (nGene) expressed across liver-resident cell lineages in healthy *versus* cirrhotic livers. **d**, Violin plot: number of total Unique Molecular Identifiers (nUMI) expressed across liver-resident cell lineages in healthy *versus* cirrhotic livers. **e**, Pie charts: proportion of cell lineage per liver sample. **f**, Box and whisker plot: agreement in expression profiles across liver samples. Pearson correlation coefficients between average expression profiles for cell in each lineage, across all pairs of samples. Black bar, median value; box edges, 25th and 75th percentiles; whiskers, range. **g**, t-SNE visualisation: liver-resident dataset per liver sample; Cirrhotic samples annotated by aetiology of underlying liver disease; NAFLD, Non-alcoholic fatty liver disease; ALD, Alcohol-related liver disease; PBC, Primary biliary cholangitis.

Extended Data Figure 2

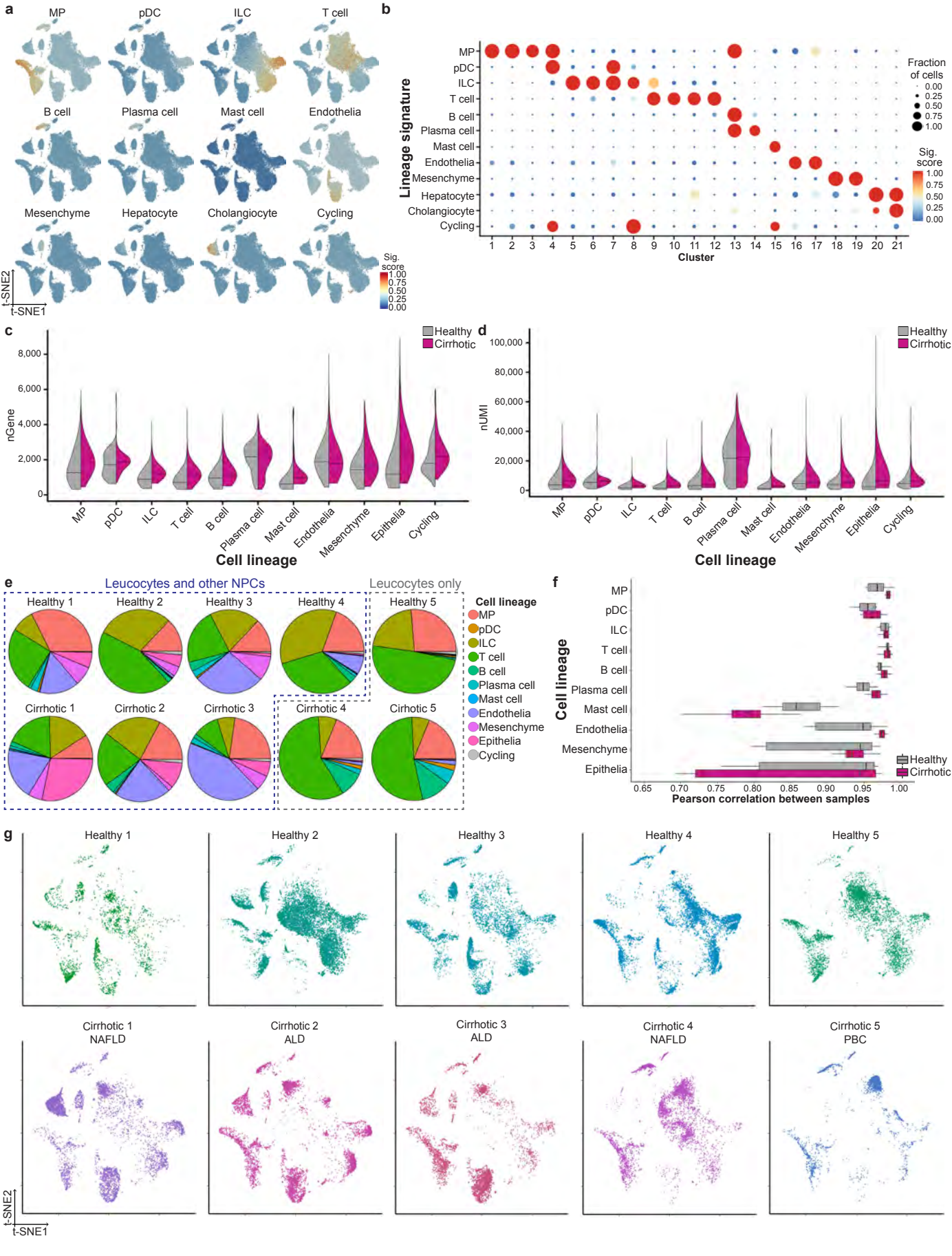

Extended Data Figure 3: Annotating human liver lymphoid cells.

a, t-SNE visualisation: clustering 36,900 T cells and innate lymphoid cells (ILC), annotating injury condition. cNK, cytotoxic NK cell. **b**, Fractions of T cell and ILC subpopulations in healthy (n=5) *versus* cirrhotic (n=5) livers, Wald. **c**, t-SNE visualisations: selected genes expressed in the T cell and ILC lineage. **d**, Scaled heatmap (red, high; blue, low): T cell and ILC cluster marker genes (colour coded top by cluster and condition), exemplar genes labelled right. Cells columns, genes rows. **e**, t-SNE visualisations: downsampled T cell and ILC dataset (7,380 cells) pre- and post-imputation; annotating data used for visualisation and clustering, inferred lineage, injury condition. No additional heterogeneity was observed following imputation. **f**, t-SNE visualisation: clustering 2,746 B cells and plasma cells, annotating injury condition. **g**, Scaled heatmap (red, high; blue, low): B cell and plasma cell cluster marker genes (colour coded top by cluster and condition), exemplar genes labelled right. Cells columns, genes rows. **h**, Fractions of B cell and plasma cell subpopulations in healthy (n=5) *versus* cirrhotic (n=5) livers, Wald. Error bars, s.e.m.; *** p-value < 0.001.

Extended Data Figure 3

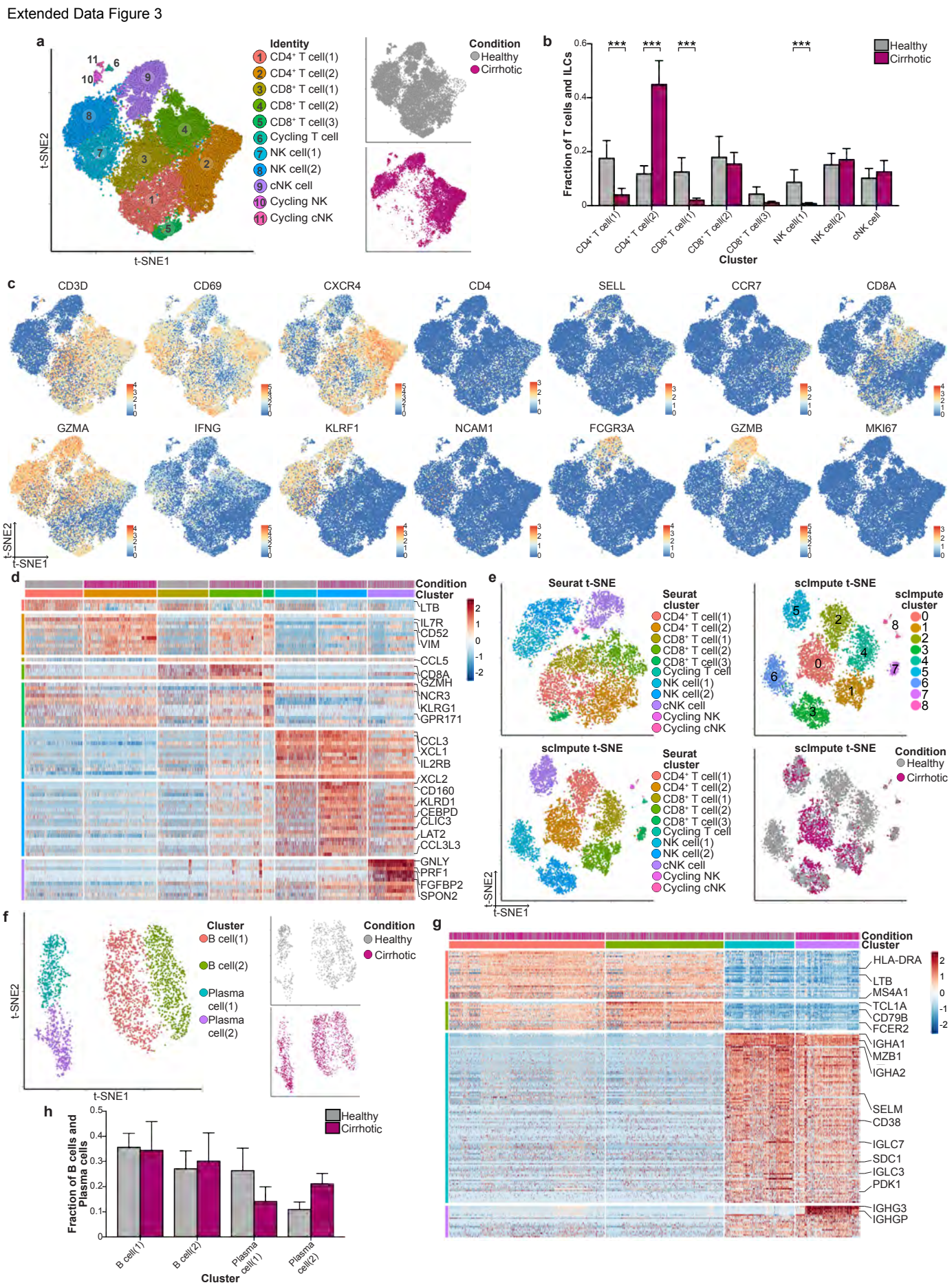

Extended Data Figure 4: Annotating human liver mononuclear phagocytes.

a, t-SNE visualisation: clustering and selected genes expressed in mononuclear phagocyte (MP) lineage. **b**, Violin plots: Kupffer cell (KC) cluster markers. **c**, Representative immunofluorescence micrograph, healthy *versus* cirrhotic liver: TIMD4 (red), CD163 (white), MARCO (green), DAPI (blue), arrows $CD163^{+}MARCO^{+}TIMD4^{-}$ cells. **d**, Automated cell counting: TIMD4 staining, healthy (n=12) *versus* cirrhotic (n=9) liver, Mann-Whitney. **e**, Automated cell counting: MARCO staining, healthy (n=8) *versus* cirrhotic (n=8) liver, Mann-Whitney. **f**, Representative flow cytometry plots: gating strategy for identifying KC, TMo and SAM. SAM are detected as TREM2+CD9+ cells within the TMo and SAM gate (see Fig. 2f). **g**, Representative immunofluorescence micrograph, cirrhotic liver: TREM2 (red), MNDA (white), collagen 1 (green), DAPI (blue). **h**, Representative micrograph, cirrhotic liver: TREM2 (smFISH; red), MNDA (immunofluorescence; green), DAPI (blue). **i**, Representative immunofluorescence micrograph, cirrhotic liver: CD9 (red), MNDA (white), collagen 1 (green), DAPI (blue). **j**, Violin plots: cycling MP cluster markers. **k**, Fractions of cycling MP subpopulations in healthy (n=5) *versus* cirrhotic (n=5) livers, Wald. Scale bars, 50µm. Error bars, s.e.m.; * p-value < 0.05, *** p-value < 0.001.

Extended Data Figure 4

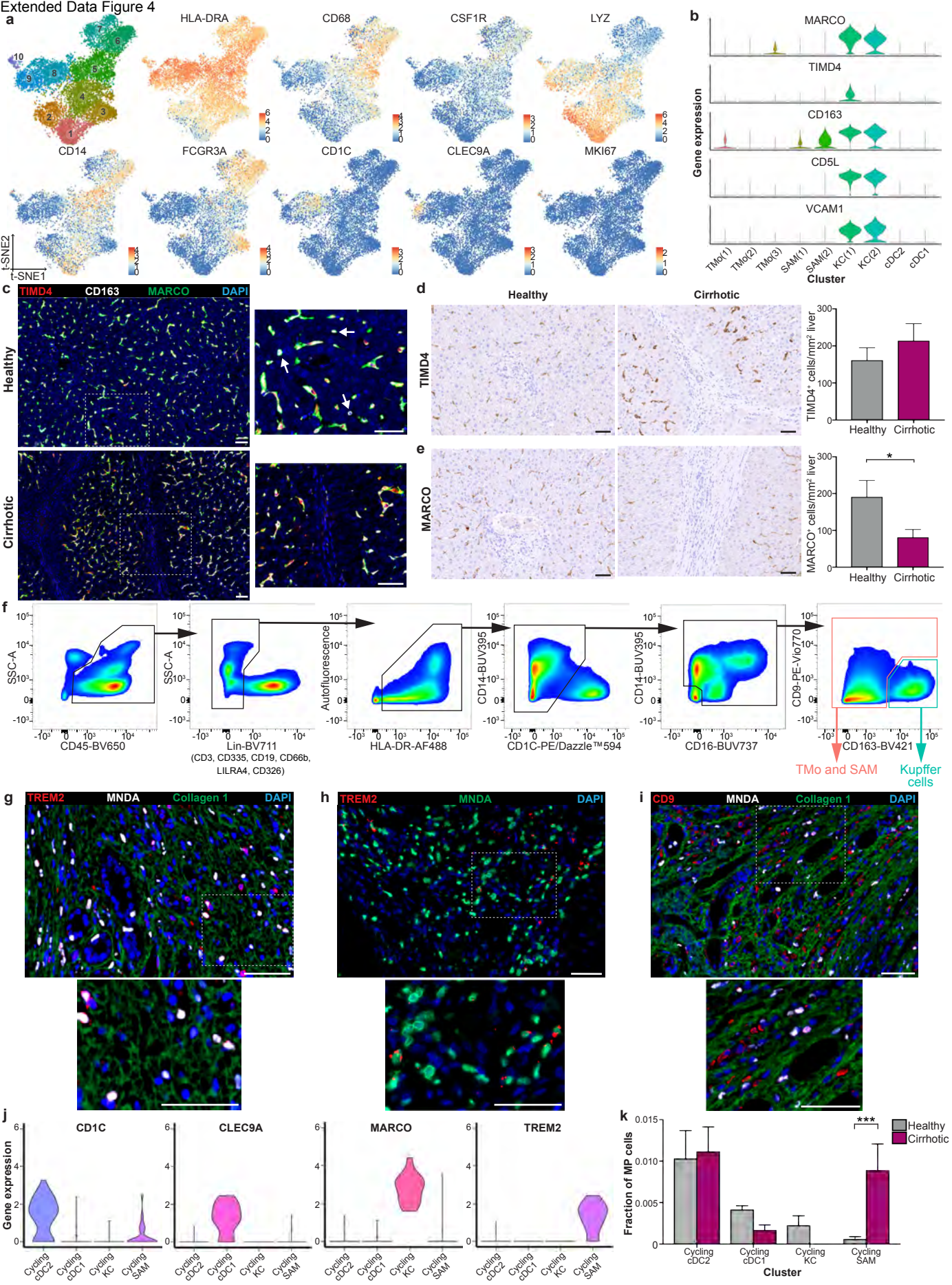

Extended Data Figure 5: Phenotypic characterisation of mononuclear phagocytes in healthy and cirrhotic human livers.

a, Self-Organising Map (SOM; 60x60 grid): smoothed mean metagene expression profile for mononuclear phagocyte (MP) subpopulations. **b**, Radar plots (left): metagene signatures D-F showing distribution of signature expression across MP subpopulations, exemplar genes (middle) and Gene Ontology (GO) enrichment (right). **c**, Luminex assay: quantification of levels of stated proteins in culture medium from FACS-isolated scar-associated macrophages (SAM, n=3), tissue monocytes (TMo, n=2), Kupffer cells (KC, n=2), and control (media alone, n=2). MFI, median fluorescence intensity. **d**, Hepatic stellate cell (HSC) activation assay: HSC treated with conditioned media from FACS-isolated SAM (n=3) or TMo (n=3); qPCR of stated genes, expression relative to mean expression of control HSC (n=6), Kruskal-Wallis and Dunn. **e**, Cubic smoothing spline curve fitted to averaged expression of all genes in module 2 from blood monocyte-SAM pseudotemporal trajectory, selected GO enrichment (right) and curves fit to exemplar genes (below). **f**, Cubic smoothing spline curve fitted to averaged expression of all genes in module 3 from blood monocyte-cDC pseudotemporal trajectory, GO enrichment (right) and curves fit to exemplar genes (below). **g**, Scaled heatmap (red, high; blue, low): transcription factor regulons across MP pseudotemporal trajectory and in KC. Colour coded top by MP cluster, condition and pseudotime, selected regulons labelled right. Cells columns, regulons rows. **h**, Violin plots: selected regulons expressed across MP clusters.

Extended Data Figure 5

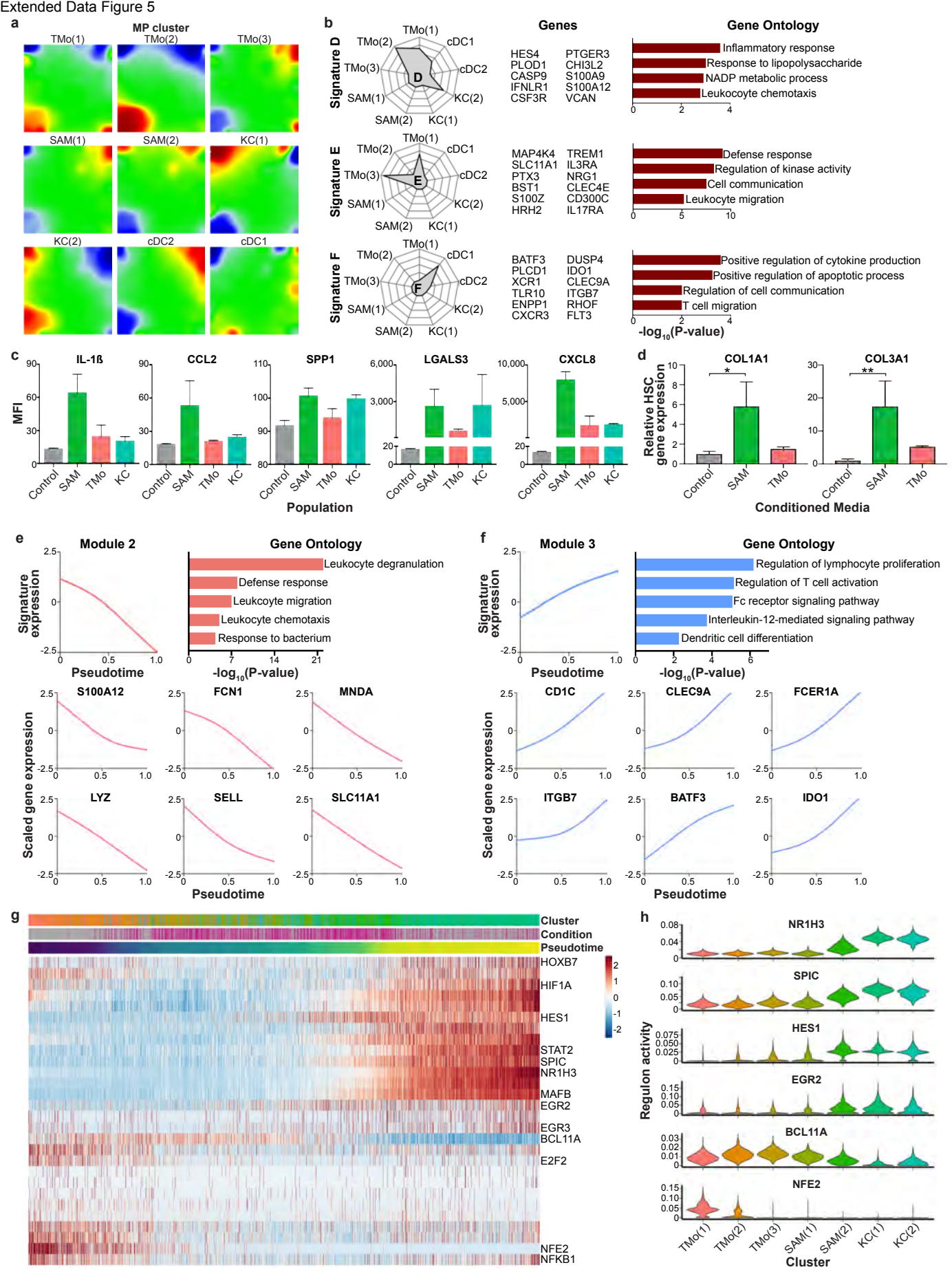

Extended Data Figure 6: Characterisation of macrophages in mouse liver fibrosis.

a, t-SNE visualisation: clustering 3,250 mouse mononuclear phagocytes (mMP) into 5 clusters (colour and number). Annotation of mouse clusters (identity). mTMo, tissue monocyte; mSAM, scar-associated macrophage; mKC, Kupffer cell; mcDC, conventional dendritic cell. **b**, t-SNE visualisation: annotating mMP cells by injury condition (colour); healthy (uninjured) or fibrotic (4 weeks carbon tetrachloride treatment). **c**, Scaled heatmap (red, high; blue, low): mMP cluster marker genes (top, colour coded by cluster and condition), exemplar genes labelled (right). Cells columns, genes rows. **d**, t-SNE visualisations: selected genes expressed in mMP. **e**, Representative flow cytometry plots: gating strategy for identifying mKC, CD9- mTMo and CD9+ mSAM. **f**, Quantifying mouse macrophage subpopulations by flow cytometry: healthy (n=6) and fibrotic (n=8) mouse liver, macrophage subpopulation (x-axis) as a percentage of total viable CD45+ cells (y-axis), Mann-Whitney. **g**, Hepatic stellate cell activation assay: co-culture of hepatic stellate cells (HSC) from uninjured mouse liver and FACS-isolated macrophage subpopulations (Mθ) from fibrotic mouse liver (left). Co-culture with CD9- mTMo (n=8) or CD9+ mSAM (n=8), qPCR of Col3a1 in HSC, expression relative to mean expression of quiescent HSC (right), Wilcoxon. **h**, t-SNE visualisation: clustering 3,250 mouse mononuclear phagocytes (mMP) and 10,737 human mononuclear phagocytes (hMP) into 5 clusters (colour and number) using canonical correlation analysis (CCA). Annotation of cross-species clusters (identity). **i**, t-SNE visualisations: human and mouse macrophage subpopulation annotation. **j**, t-SNE visualisations: selected genes expressed in cross-species clusters. Error bars, s.e.m.; ** p-value < 0.01; *** p-value < 0.001.

Extended Data Figure 6

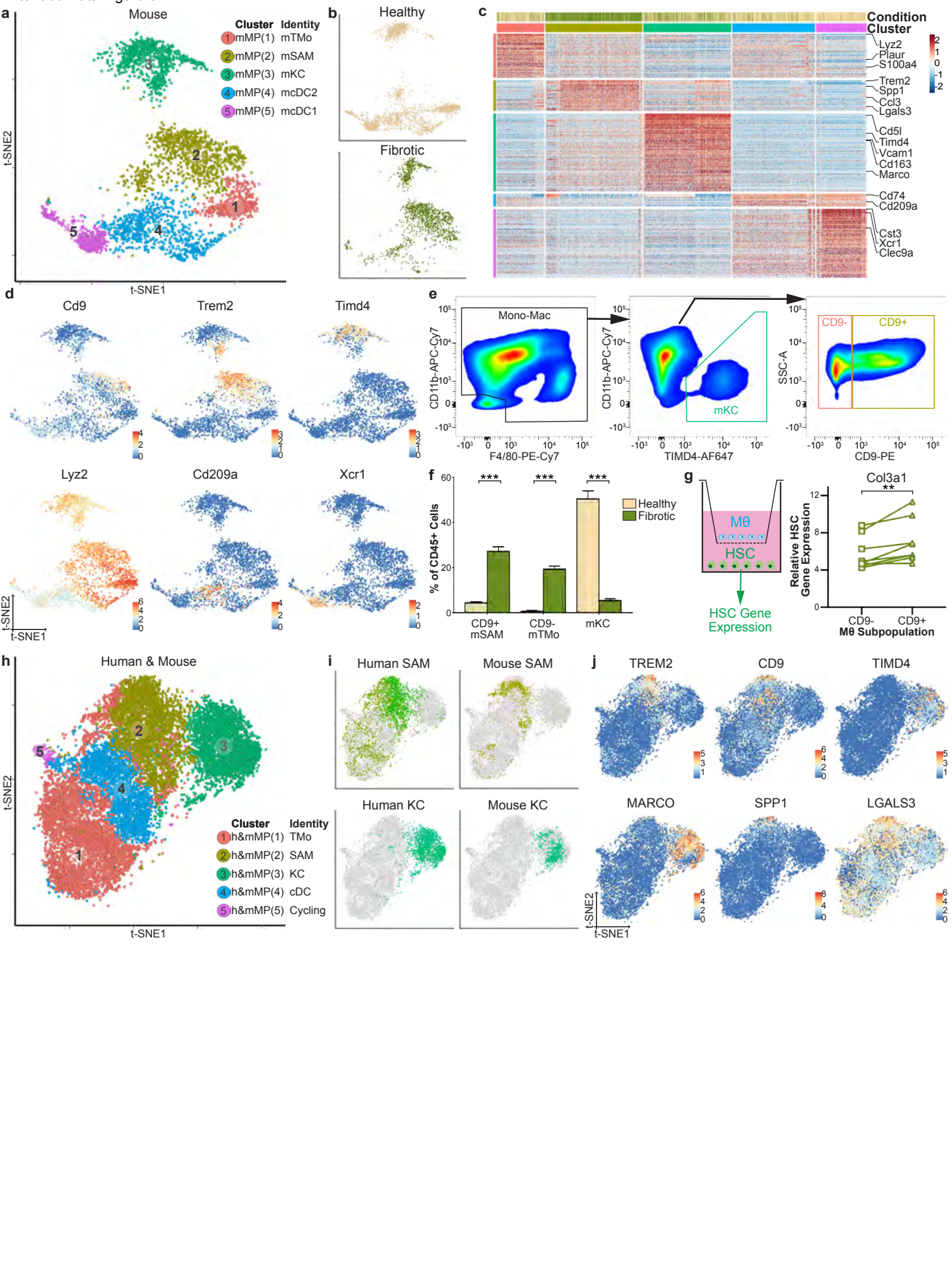

Extended Data Figure 7: Scar-associated macrophage expansion in human NASH

a to d, Deconvolution: publicly available whole liver microarray data (n=73) assessed for frequency of scar-associated macrophages (SAM), Kupffer cells (KC) and tissue monocytes (TMo) using Cibersort algorithm. **a**, Macrophage composition: x-axis, GEO accession number; y-axis, fraction of monocyte-macrophages; Top, annotated by liver phenotype; NASH, Non-alcoholic steatohepatitis. **b**, Frequency of SAM in control (n=14), heathy obese (n=27), steatosis (n=14) and NASH (n=18) livers, Kruskal-Wallis and Dunn. **c**, Frequency of SAM in patients with histological NAFLD activity score (NAS) of 0 (n=37), 1-3 (n=19) and 4-7 (n=17) (left). Frequency of SAM in patients with histological fibrosis score of 0 (n=46), 1 (n=20) and 2-4 (n=5) (right), Kruskal-Wallis and Dunn. **d**, Frequency of SAM in female (n=58) and male (n=15) patients (left). Frequency of SAM in patients aged 23-39 (n=22), 40-49 (n=29) and 50-80 (n=22) (middle). Frequency of SAM in patients with a body mass index (BMI) of 17-30 (n=18), 31-45 (n=28) and 46-70 (n=27) (right). All Kruskal-Wallis and Dunn. **e**, CD9 and TREM2 staining in NASH liver biopsy sections (left). Automated cell counting (right): CD9 staining, NAS 1-3 (n=13) *versus* NAS 4-8 (n=21). TREM2 staining, NAS 1-3 (n=12) *versus* NAS 4-8 (n=16), Mann-Whitney. **f**, Correlation of automated cell counts with picrosirius red (PSR) digital morphometric pixel quantification in NAFLD liver biopsy tissue; CD9 staining (top; n=39); TREM2 staining (bottom; n=32); Pearson correlation and linear regression. Scale bars, 50μm. Error bars, s.e.m.; * p-value < 0.05, ** p-value < 0.01.

Extended Data Figure 7

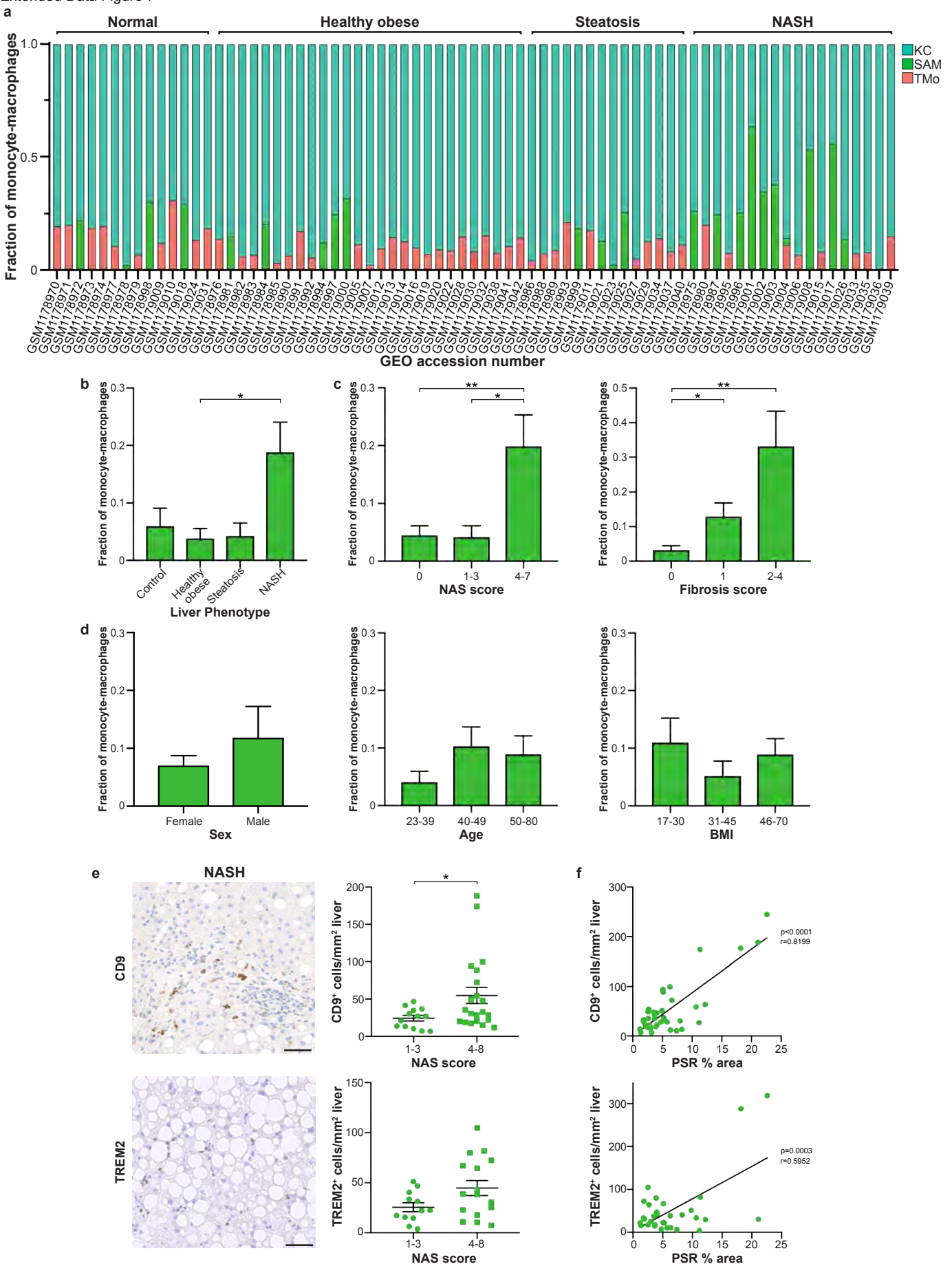

Extended Data Figure 8: Phenotypic characterisation of endothelial cells in healthy and cirrhotic human livers.

a, t-SNE visualisations: clusters and selected genes expressed in endothelial lineage. **b**, Violin plots: endothelial cluster marker genes. **c**, Digital morphometric pixel quantification: PLVAP stained cirrhotic sections (n=10) morphologically segmented into fibrotic septae and parenchymal nodules (top); ACKR1 stained cirrhotic sections (n=10) morphologically segmented into fibrotic septae and parenchymal nodules (bottom), Wilcoxon. **d**, Flow cytometry: endothelial cells from healthy (n=3) or cirrhotic (n=7) liver, representative histogram for stated marker (top), mean fluorescence intensity (MFI, bottom), Mann-Whitney. **e**, Flow-based adhesion assay: peripheral blood monocytes were assessed for adhesion (left) and % of adherent cells which transmigrate (right); endothelial cells from healthy (n=5) or cirrhotic (n=4) liver, Mann-Whitney. **f**, Endothelial cell gene knockdown: cirrhotic endothelial cells treated with siRNA to PLVAP (n=6), ACKR1 (n=5) or control siRNA (n=6). Representative flow cytometry histograms for stated marker (top); comparison to isotype control antibody. Flow-based adhesion assay (bottom), peripheral blood mononuclear cells assessed for adhesion (bottom left) and % of adherent cells which transmigrate (bottom right) following siRNA treatment of endothelial cells, Kruskal-Wallis and Dunn. **g**, Self-Organising Map (SOM; 60 x 60 grid; top left): smoothed scaled metagene expression of endothelia lineage. 21,237 genes, 3,600 metagenes, 45 signatures. A-E label metagene signatures overexpressed in one or more endothelial subpopulations. SOM: smoothed mean metagene expression profile for each endothelial subpopulation (top right). Radar plots (bottom left): metagene signatures A-E showing distribution of signature expression across endothelial subpopulations, exemplar genes (bottom middle) and Gene Ontology (GO) enrichment (bottom right). **h**, t-SNE visualisation: endothelia subpopulation annotation, injury condition. **i**, t-SNE visualisation: endothelial lineage annotated by *monocle* pseudotemporal dynamics (purple to yellow; grey indicates lack of inferred trajectory). RNA velocities (red arrows) visualised using Gaussian smoothing on regular grid. Error bars, s.e.m.; * p-value<0.05; ** p-value < 0.01.

Extended Data Figure 8

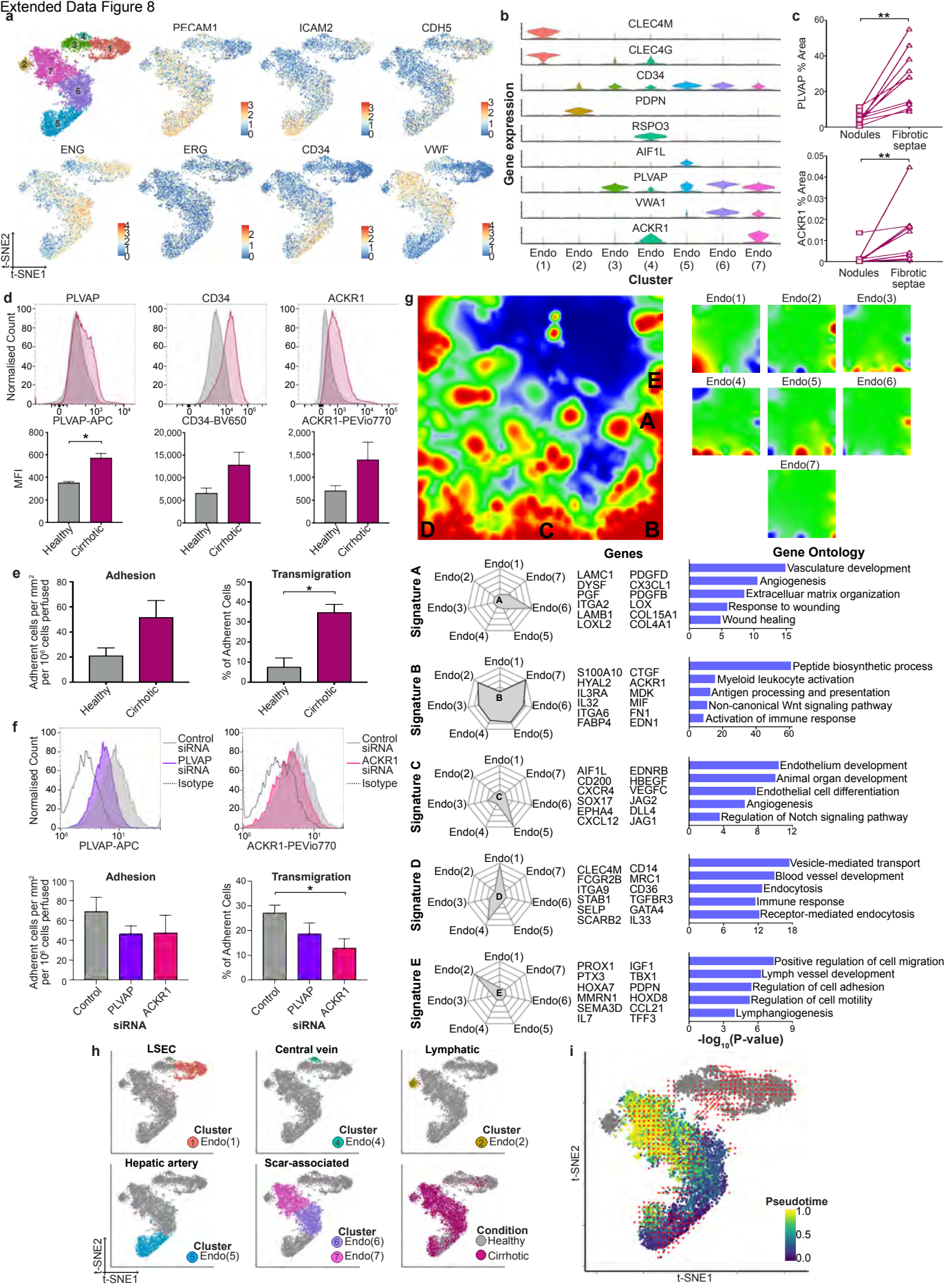

Extended Data Figure 9: Characterisation of mesenchymal cells in healthy and cirrhotic human livers.

a, t-SNE visualisations: selected genes expressed in mesenchymal lineage. **b**, t-SNE visualisation: clustering 319 scar-associated mesenchymal cells (SAMes), into 2 further subclusters (colour and number). **c**, Scaled heatmap (red, high; blue, low): SAMes subcluster marker genes (top, colour coded by cluster and condition), exemplar genes labelled (right). Cells columns, genes rows. **d**, Fractions of SAMes subpopulations in healthy (n=4) *versus* cirrhotic (n=3) livers, Wald. **e**, Representative immunofluorescence micrograph, portal region of healthy liver: OSR1 (red), Collagen 1 (green), DAPI (blue). **e**, Representative immunofluorescence micrograph, fibrotic niche of cirrhotic liver: OSR1 (red), Collagen 1 (green), DAPI (blue). **g**, t-SNE visualisation: Hepatic stellate cell (HSC) and SAMes clusters annotated by *monocle* pseudotemporal dynamics (purple to yellow). RNA velocity field (red arrows) visualised using Gaussian smoothing on regular grid. **h**, Scaled heatmap (red, high; blue low): cubic smoothing spline curves fitted to genes differentially expressed across HSC-to-SAMes pseudotemporal trajectories, grouped by hierarchical clustering (k=2). Colour coded by pseudotime and condition (top). Gene co-expression modules (colour) and exemplar genes labelled right. Scale bars, 50μm. Error bars, s.e.m.; *** p-value < 0.001.

Extended Data Figure 9

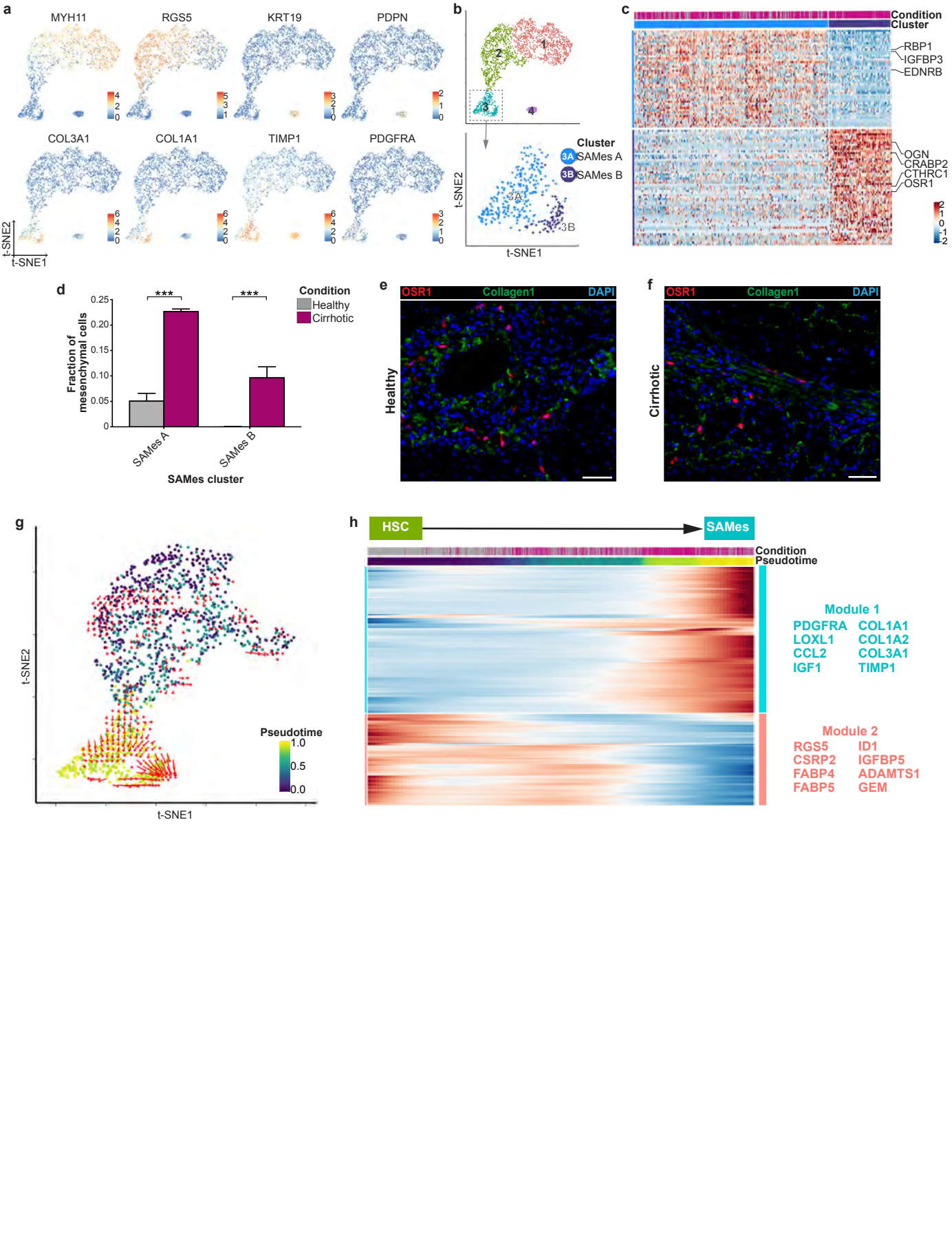

Extended Data Figure 10: Characterisation of the cellular interactome in the fibrotic niche.

a, Circle plot: potential interaction magnitude from ligands expressed by scar-associated macrophages (SAM) and endothelial cells (SAEndo) to receptors expressed on scar-associated mesenchyme (SAMes). **b**, Circle plot: potential interaction magnitude from ligands expressed by SAMes to receptors expressed on SAM and SAEndo. **c**, Dotplot: ligand-receptor interactions between SAMes, SAM and SAEndo. X-axis, ligand (red) and cognate receptor (blue); y-axis, ligand (red) and receptor (blue) expressing cell populations; circle size, p-value; colour (red, high; yellow, low), means of average ligand and receptor expression levels in interacting subpopulations. **d**, Representative immunofluorescence micrographs, fibrotic niche in cirrhotic liver. Top; CCL2 (red), CCR2 (white), PDGFRα (green), DAPI (blue), arrows $CCL2^{+}PDGFR\alpha^{+}$ cells. Bottom; ANGPT1 (red), TEK(white), PDGFRα (green), DAPI (blue), arrows $ANGPT1^{+}PDGFR\alpha^{+}$ cells. **e**, Circle plot: potential interaction magnitude from ligands expressed by SAM to receptors expressed on SAEndo. **f**, Dotplot: ligand-receptor interactions between SAM and SAEndo. X-axis, ligand (red) and cognate receptor (blue); y-axis, ligand (red) and receptor (blue) expressing cell populations; circle size, p-value; colour (red, high; yellow, low), means of average ligand and receptor expression levels in interacting subpopulations. **g**, Representative immunofluorescence micrographs, fibrotic niche in cirrhotic liver. TREM2 (red), FLT1 (white), VEGFA (green), DAPI (blue), arrows $TREM2^{+}VEGFA^{+}$ cells. **h**, Circle plot: potential interaction magnitude from ligands expressed by SAEndo to receptors expressed on SAM. **i**, Dotplot: ligand-receptor interactions between SAEndo and SAM. X-axis, ligand (red) and cognate receptor (blue); y-axis, ligand (red) and receptor (blue) expressing cell populations; circle size, p-value; colour (red, high; yellow, low), means of average ligand and receptor expression levels in interacting subpopulations. **j**, Representative immunofluorescence micrographs, fibrotic niche in cirrhotic liver. Top; TREM2 (red), CD200 (white), CD200R (green), DAPI (blue), arrows $TREM2^{+}CD200R^{+}$ cells. Bottom; TREM2 (red), DLL4 (white), NOTCH2 (green), DAPI (blue), arrows $TREM2^{+}NOTCH2^{+}$ cells. Scale bars, 50μm.

Extended Data Figure 10